



**HAL**  
open science

## Porosity, permeability and 3D fracture network characterisation of dolomite reservoir rock samples

M. Voorn, U. Exner, A. Barnhoorn, P. Baud, T. Reuschlé

### ► To cite this version:

M. Voorn, U. Exner, A. Barnhoorn, P. Baud, T. Reuschlé. Porosity, permeability and 3D fracture network characterisation of dolomite reservoir rock samples. *Journal of Petroleum Science and Engineering*, 2015, 127, pp.270-285. 10.1016/j.petrol.2014.12.019 . hal-01253012

**HAL Id: hal-01253012**

**<https://hal.science/hal-01253012v1>**

Submitted on 14 Oct 2024

**HAL** is a multi-disciplinary open access archive for the deposit and dissemination of scientific research documents, whether they are published or not. The documents may come from teaching and research institutions in France or abroad, or from public or private research centers.

L'archive ouverte pluridisciplinaire **HAL**, est destinée au dépôt et à la diffusion de documents scientifiques de niveau recherche, publiés ou non, émanant des établissements d'enseignement et de recherche français ou étrangers, des laboratoires publics ou privés.

Published in final edited form as:

*J Pet Sci Eng.* 2015 March 1; 127(March): 270–285. doi:10.1016/j.petrol.2014.12.019.

## Porosity, permeability and 3D fracture network characterisation of dolomite reservoir rock samples

Maarten Voorn<sup>a,\*</sup>, Ulrike Exner<sup>b</sup>, Auke Barnhoorn<sup>c</sup>, Patrick Baud<sup>d</sup>, and Thierry Reuschlé<sup>d</sup>

<sup>a)</sup> Department of Geodynamics and Sedimentology, University of Vienna, Althanstrasse 14, 1090 Vienna, Austria <sup>b)</sup> Natural History Museum, Department of Geology and Palaeontology, Burgring 7, 1010 Vienna, Austria <sup>c)</sup> Department of Geoscience and Engineering, Delft University of Technology, Stevinweg 1, 2628 CN Delft, The Netherlands <sup>d)</sup> Laboratoire de Déformation des Roches, Équipe de Géophysique Expérimentale, Institut de Physique de Globe de Strasbourg (UMR7516 CNRS, Université de Strasbourg/EOST), 5 rue René Descartes, 67084 Strasbourg cedex, France

### Abstract

With fractured rocks making up an important part of hydrocarbon reservoirs worldwide, detailed analysis of fractures and fracture networks is essential. However, common analyses on drill core and plug samples taken from such reservoirs (including hand specimen analysis, thin section analysis and laboratory porosity and permeability determination) however suffer from various problems, such as having a limited resolution, providing only 2D and no internal structure information, being destructive on the samples and/or not being representative for full fracture networks. In this paper, we therefore explore the use of an additional method – non-destructive 3D X-ray micro-Computed Tomography ( $\mu$ CT) – to obtain more information on such fractured samples. Seven plug-sized samples were selected from narrowly fractured rocks of the Hauptdolomit formation, taken from wellbores in the Vienna basin, Austria. These samples span a range of different fault rocks in a fault zone interpretation, from damage zone to fault core. We process the 3D  $\mu$ CT data in this study by a Hessian-based fracture filtering routine and can successfully extract porosity, fracture aperture, fracture density and fracture orientations – in bulk as well as locally. Additionally, thin sections made from selected plug samples provide 2D information with a much higher detail than the  $\mu$ CT data. Finally, gas- and water permeability measurements under confining pressure provide an important link (at least in order of magnitude) towards more realistic reservoir conditions.

This study shows that 3D  $\mu$ CT can be applied efficiently on plug-sized samples of naturally fractured rocks, and that although there are limitations, several important parameters can be extracted.  $\mu$ CT can therefore be a useful addition to studies on such reservoir rocks, and provide valuable input for modelling and simulations. Also permeability experiments under confining pressure provide important additional insights. Combining these and other methods can therefore be a powerful approach in microstructural analysis of reservoir rocks, especially when applying

---

\* maarten.voorn@univie.ac.at

ulrike.exner@nhm-wien.ac.at, auke.barnhoorn@tudelft.nl, patrick.baud@unistra.fr, thierry.reuschle@unistra.fr

the concepts that we present (on a small set of samples) in a larger study, in an automated and standardised manner.

## Keywords

$\mu$ CT; Computed tomography; Image processing; Aperture; Permeability; Confining pressure

---

## 1. Introduction

Fractured reservoirs constitute a significant part of the world's hydrocarbon potential. As pointed out by Nelson (2001), the presence and topology of natural fractures in reservoirs have been and are too often ignored or oversimplified in their interpretation, leading to wrong decisions in exploration and production plans. Natural fractures cannot only contain significant volumes of hydrocarbons (connected porosity), but are in many reservoirs vital for allowing flow at sufficient rates for production (permeability), so analysing and understanding the complexity of fractures and fracture networks is crucial. Nelson (2001) and Aguilera (1995) have given excellent overviews of fractured reservoirs, their characteristics, and their analysis over a wide range of geological scales. In this paper, we will focus on fracture analyses at the scale of drill cores and plugs, and some common analyses will be discussed first.

After recovery, initial research on drill cores and plugs is mostly done at hand specimen scale, in the form of core logs. At this scale, for example composition, fracture density and orientation can be determined, and may sometimes be compared to features observable at the scale of borehole logs and borehole imaging logs (e.g. microresistivity by Formation MicroImaging (FMI); Ekstrom et al., 1987; Prensky, 1999). However, the resolution of the above techniques is limited, and no details about the internal structure of the reservoir rocks can be obtained.

After hand specimen analysis, cores and smaller drilled out plugs are selected to determine their (among others) porosity and permeability, using standardised methods in the laboratory (e.g. API, 1998; Andersen et al., 2013). Such laboratory measurements are also used in this study, but as they provide bulk values only, no information about the internal structure of a core or plug sample is obtained. Some laboratory methods like Mercury Intrusion Porosimetry (MIP; e.g. Klobes et al., 1997; API, 1998; Andersen et al., 2013) do provide information about the internal structure of samples, but are invasive in nature, and samples may not be suitable anymore for other analyses afterwards.

Following bulk laboratory measurements, thin section analysis on drill core samples and wall cuttings can be carried out, if a more detailed analysis of their internal structure is required (e.g. Anselmetti et al., 1998; Gale et al., 2004). Thin sections provide very detailed, generally two-dimensional views of the microstructure of the rocks, and are therefore still an important part of our research. However, creating thin sections is destructive on the original samples, and the 2D view can be limiting, especially when looking at fracture networks.

Finally, several (less common) analyses can potentially be carried out to characterise fractures on the core and plug scale. For example, fracture surface, fracture roughness and fracture aperture have been analysed in the past using varying methods (for example by physical and optical surface profiling, Plouraboué et al., 1995; Isakov et al., 2001; Kulatilake et al., 2008; Sharifzadeh et al., 2008; Neuville et al., 2012; overview of methodologies in Hakami et al., 1995). These methods are very detailed and are usually only applied on single (often artificially created) fractures, so are not well applicable on fracture networks. Another option is to generate theoretical models of fracture networks, by applying stochastic methods to create fractures with realistic spacing, connectivity, aperture and flow properties (for example Discrete Fracture Networks, e.g. Singhal & Gupta, 2010; Sahimi, 2011). Such methods are especially useful at the reservoir scale, but may not be fully representative for the actual situation and complexity found in nature, and they still require realistic input data (e.g. obtained by the methods listed before).

The mentioned methods of conventional research on fractured core and plug samples thus all have at least one of the following drawbacks: (1) a limited level of detail for fracture characterisation, (2) limited or no information on the internal structure, (3) two-dimensional information only, (4) destructive on the samples, (5) not applicable on, or not representative for full fracture networks. A good candidate for overcoming these drawbacks is X-ray micro-Computed Tomography ( $\mu$ CT), which allows us to non-destructively image samples in 3D in detail, and thereby allows us to extract properties that otherwise would remain uncovered (for example fracture connectivity, fracture aperture, fracture orientation). Although the use of  $\mu$ CT has its own drawbacks and limitations (discussed later), it provides a good compromise between the 5 drawbacks mentioned above, especially when complemented with other analytical methods.

CT and  $\mu$ CT are nowadays commonly used in various branches of geosciences. For an overview on ( $\mu$ )CT scanning, applications in the geosciences, and important parameters and processing steps to consider, the reader is referred to Ketcham and Carlson (2001), Mees et al. (2003), Cnudde et al. (2006) and Kaestner et al. (2008). Quite some ( $\mu$ )CT research has been carried out on samples containing fractures (e.g. Keller, 1998; Bertels et al., 2001; Van Geet & Swennen, 2001; Sellers et al., 2003; Muralidharan et al., 2004; Karpyn et al., 2007; Zabler et al., 2008; Wennberg et al., 2009; Watanabe et al., 2011; Ellis, 2012). These papers cover a wide range of lithologies, scales, and ( $\mu$ )CT processing and analysis routines. Unfortunately, they focus only on single fractures or relatively simple combinations of fractures. ( $\mu$ )CT has occasionally been applied on more complex (natural) fracture networks, with some examples in literature: on building materials (Landis et al., 2003; Ehrig et al., 2011), coals and clays (Montemagno & Pyrak-Nolte, 1999; Bossie-Codreanu et al., 2004; Lenoir et al., 2007) as well as on carbonates (Christe, 2009; Barnhoorn et al., 2010; Zalewska et al., 2011; Fusi & Martinez-Martinez, 2013; Jia et al., 2013). One of the main obstacles throughout this literature is the efficient 3D processing and analysis of fractures, and especially of narrow fractures. An important focus of this study lies therefore on the extraction of narrow fracture networks and other porous structures from  $\mu$ CT data, using a Hessian-based filtering technique for planar features introduced by Voorn et al. (2013). After this processing step, we focus on the determination of important parameters for the

hydrocarbon industry, such as porosity, fracture aperture, fracture density and fracture orientation.

The main question we try to answer here is how to efficiently analyse natural fracture networks in dense rocks, using various methods (2D and 3D imaging, and laboratory porosity and permeability determination), with an emphasis on 3D  $\mu$ CT. These descriptions will be primarily based on 7 dolomite plug samples from the basement of the Vienna Basin (Austria), with different fracture and porosity characteristics. The above methods are however all applied at surface conditions. To obtain a better understanding of the behaviour of the samples at depth, we also subjected most plug samples to permeability experiments under confining pressure. Combined with the imaging information on structure, this can serve as an important input for permeability and reservoir modelling.

## 2. Geological background and samples

The rocks analysed in this study originate from the Upper Triassic (Norian) Hauptdolomit (Dolomia Principale in Italian-speaking regions) formation, a major formation present throughout the Alps and built up of mainly dolostone. In literature, the rocks of the Hauptdolomit formation are consistently thought to have formed by syn-sedimentary or very early dolomitisation (e.g. Fruth & Scherreiks, 1984; Blendinger, 1997; Masaryk & Lintnerová, 1997; Antonellini & Mollema, 2000; Meister et al., 2013), and are affected by partial dedolomitisation in some areas (Masaryk & Lintnerová, 1997).

All samples in this study are taken from cores from wells drilled in the pre-Neogene basement of the Vienna Basin (Austria), with the depths of origin listed in Table 1. In the Vienna Basin basement, the Hauptdolomit formation rocks are present in different tectonic nappes of the Northern Calcareous Alps (NCA), with the NCA itself being a component of the larger allochthonous Alpine-Carpathian thrust complex. Both the Alpine nappe stacking in this thrust complex up to the end of the Paleogene, and the formation of the Vienna Basin by pull-apart extension from the Early Neogene (Miocene) onwards, have affected the Hauptdolomit rocks (Zimmer & Wessely, 1996; Arzmüller et al., 2006), leading to a complex dense fracture network over a wide range of scales (Peresson & Decker, 1997). From these densely fractured rocks, hydrocarbon (mainly gas) exploration and production have been successful since the early 1960s (Zimmer & Wessely, 1996). However, some of these reservoirs produce better than others, and the reasons for this are not always well understood. Because several of the wells are quite old (drilled in the 1960s and 1970s), logging information is not as extensive as for more modern wellbores, and is therefore not always useful for detailed microstructural analysis. The information gathered from  $\mu$ CT imaging may therefore help to understand the rocks – and the differences between the reservoirs – in a better way.

To place our results into a better perspective than from the core alone, we adopt a classification scheme for fault rocks based on fieldwork studies (Figures 1a and 7a). Most fault zones in carbonate rocks are characterised by a fault core, surrounded by a damage zone (e.g. Billi et al., 2003). In dolomite rocks of the Hauptdolomit and similar formations, there is usually a single master fault containing the most intensely damaged rocks (Bauer,

2010; Schröckenfuchs, 2012). Furthest away from this master fault, virtually undamaged rocks are present. When moving towards the fault core, the fracture density increases, up to a point where the rock contains fractures with varying orientations and a spacing of less than 1 cm (Figure 1b-d). Again further towards the fault core, a transition zone characterised by mosaic breccias with partial calcite cementation is found (Woodcock et al., 2006; Figure 1e-g). Finally, after the transition zone, the actual fault core is characterised by cataclasites, where the degree of cataclasis tends to increase when getting closer to the master fault (Figure 1h-j). A distinction can be made here between embryonic (<50% matrix), intermediate (50-80% matrix) and mature cataclasites (>80% matrix), although it is not always possible to unequivocally distinguish between the cataclasite types (Billi, 2010). The boundary between matrix and grains is set at 4  $\mu\text{m}$  in this classification (Flügel, 2004).

Because we investigate core samples only, any inference of their relationship to the overall fault zone is somewhat interpretive. We thus stress that the used classification is mainly a tool to discriminate among the rocks types we observe, and not a definite claim that the rocks in question came from a certain part of the zone. Additionally, we can only sample rocks containing enough porosity and fractures to visualise using  $\mu\text{CT}$ , but do not readily disintegrate upon sample acquisition or analysis. This of course may introduce an (unavoidable) bias in the sampling, to which we will return in the discussion. Finally, it is likely the samples underwent some changes due to unloading during drilling, and we cannot exclude the presence of some drilling-induced fractures completely. However, no clear indications for induced fractures as listed by Nelson (2001) were observed.

The 7 dolomite plug samples scanned using  $\mu\text{CT}$  are listed in Table 1, according to their fault zone interpretation and including details on dimensions, depth, texture, cements and clay content.

### 3. 3D and 2D imaging methods

#### 3.1. 3D X-Ray micro-Computed Tomography ( $\mu\text{CT}$ )

**3.1.1.  $\mu\text{CT}$  scanning details**—The plug samples listed in Table 1 were scanned using a Rayscan 250E X-ray micro-Computed Tomography ( $\mu\text{CT}$ ) scanner at the Research Group Computed Tomography of the University of Applied Sciences of Upper Austria (Fachhochschule Oberösterreich, FHOÖ) in Wels, Austria. The used X-ray source is a 225 kV Viscom XT9225 DED microfocus X-ray tube with a minimum focal spot of circa 8  $\mu\text{m}$ , and the device is equipped with a 2048 $\times$ 2048 pixels 16 bit a-Si flatbed detector (of 41 $\times$ 41 cm). A copper pre-filter of 0.5 to 1.5 mm thickness (depending on the sample size) was used to reduce beam hardening effects. Source voltages of 120-165 kV were selected (hence resulting in maximum X-ray energies of 120-165 keV), and current and exposure time were adjusted empirically to ensure the best radiogram images. For all samples, between 1080 and 1800 projections were taken, and 4 to 5 radiograms of the same projection (i.e. same sample orientation in the scanner) were averaged. Although this averaging increases scanning time, it results in a much better image quality with less noise. After scanning, the data was reconstructed (i.e. calculating a 3D image volume from the 2D radiograms) with a filtered back-projection algorithm using the devices' included Rayscan reconstruction software, with a resolution of (12.5  $\mu\text{m}$ )<sup>3</sup> (2 cm diameter samples) up to (20  $\mu\text{m}$ )<sup>3</sup> (3 cm diameter samples)

per voxel. The data does not contain severe ring artefacts and only minor software beam hardening reduction (in the proprietary Rayscan software) was applied, in case the copper prefilter was insufficient. The averaging of multiple scans prevented the use of additional filters such as median filtering.

Additionally to the plug samples of Table 1, several other samples were scanned, including scans on different  $\mu$ CT scanners. Most of these scans were unsuccessful due to various reasons, such as too little structure being visible at the  $\mu$ CT resolution, or too much noise being present in the final reconstructed result. In this process, we also attempted to scan larger core samples, of 6 and 10 cm in diameter. However, X-ray penetration turns out to be insufficient at the energy levels mentioned, and higher energy settings are no option due to a decline in resolution, which would make visualisation of the narrow fractures in these samples impossible.

**3.1.2.  $\mu$ CT data processing: MSHFF filtering and segmentation**—As indicated in the introduction, processing  $\mu$ CT data – especially when containing narrow features relative to the resolution – can be problematic. The most promising approaches currently available in literature attempt to automatically fit a point spread function (PSF) to the  $\mu$ CT data in order to calculate the actual size of visible features (e.g. fracture aperture), often using a physical calibration (Ketcham et al., 2010; Ketcham & Hildebrandt, 2014). Such techniques are unfortunately still difficult to apply automatically – due to computational reasons – on full datasets with complex features, such as a fracture network. We therefore chose to apply a 3D voxel-based segmentation, using the multiscale Hessian fracture filter (MSHFF) of Voorn et al. (2013) – based on the approach for vessel filtering by Frangi et al. (1998). The MSHFF method has been implemented as macro code for the open-source software FIJI (Schindelin et al., 2012) – using the FeatureJ plugin (Meijering, 2010) for the calculation of the Hessian matrices – and runs on a desktop computer for the datasets displayed in this paper, without having to downsample these datasets first. The technical details and examples of segmentation results on fractured dolomite rocks are shown in Voorn et al. (2013). This routine has been slightly altered: the results of different Gaussian scales are multiplied with a factor  $(2/\text{scale})$  before being combined, thereby enhancing the relative strength of the narrowest features in the combined result, without compromising the detection of larger features. An example of the filtering result is shown in Figure 2b. This result is suitable for binarisation by a global threshold applied on the entire filtered dataset (Figure 2c), as the Hessian filtering method removed local greyscale variations and most noise effects. Therefore, more sophisticated binarisation techniques, such as 3D region growing, do not provide clear advantages over global thresholding compared to their computational cost, and the need for additional user choices such as seed point definition and growing guidelines (in the case of region growing). In the segmented dataset, most remaining noise is finally removed by an island filtering approach (clusters of less than 20 connected voxels in a 27-connected geometry are discarded). The final binary segmentation using the MSHFF makes it easier to analyse the data afterwards and perform further calculations on them.

### 3.1.3. $\mu$ CT data analysis

**3.1.3.1. Porosity:** After binary segmentation, the bulk porosity is determined by dividing the amount of voxels assigned to be porous by the total amount of voxels in the dataset, and normalising to 100%. Of course, the value of the porosity is very dependent on the initial data quality, resolution (e.g. no microporosity can be detected at the  $\mu$ CT scanning resolution), the filtering process and the final segmentation result, and does hence partially reflect the choices made by the operator. This is however a problem for most available segmentation routines (with some performing better than others, e.g. Sezgin & Sankur, 2004; Iassonov & Tuller, 2010).

**3.1.3.2. Aperture:** Apertures and aperture distributions have been extracted before from  $\mu$ CT data using calibration approaches, without needing to segment the data first (e.g. Keller, 1998; Montemagno & Pyrak-Nolte, 1999; Muralidharan et al., 2004; Ketcham et al., 2010). Such calibration approaches are however generally difficult to run on fracture networks, and suitable calibration samples and additional  $\mu$ CT scanning time is required for the calibration. We will therefore work with the segmented  $\mu$ CT data instead, although this does of course involve possible bias by the segmentation routine. Separating the distinct fractures in the complex fracture networks shown in this study is difficult (if not impossible), and apertures clearly vary along the fractures, leaving little meaning for single aperture values per fracture. Alternatively, the aperture distribution for the full sample is determined, using the *Local Thickness* plugin (Dougherty & Kunzelmann, 2007) for FIJI. Similar approaches with different implementations can be found in literature (e.g. Yang et al., 2009 for MATLAB (The Mathworks, Inc., 2011)), but the Local Thickness plugin was the easiest to apply on large datasets. In this approach the largest possible spheres (thus 3D) are fitted at every location inside the porous features in the previously segmented dataset (see Figure 3), as for fractures the diameter of the spheres represents aperture at the location of the sphere. The full sample's aperture distribution is displayed in a histogram. We divide the distribution by the volume of each sphere size, to compensate for volume bias (i.e. larger spheres contain many more voxels), and finally multiply the aperture distribution in voxels with the  $\mu$ CT scanning resolution. Of course, differences in resolution of  $\mu$ CT scans also affect what can be detected in terms of (especially minimum) aperture.

**3.1.3.3. Fracture density:** Fracture density can be expressed in various ways, depending on the analysis method and scale. For the samples shown here we apply one of the simplest bulk definitions available in literature: fracture density [ $\text{m}^{-1}$ ] = total fracture surface [ $\text{m}^2$ ] / sample volume [ $\text{m}^3$ ] (Singhal & Gupta, 2010). Fracture surface is estimated from the results of the aperture determination approach. We assume the total number of voxels in an aperture size class (=volume) can be divided by its aperture (=length, in voxels) – to provide the fracture surface of that aperture size class – and sum these. This assumption can be made for fractures since the fitted spheres of the aperture determination approach overlap completely. The  $\mu$ CT scanning resolution is used to convert the fracture density to the proper units of  $\text{m}^{-1}$ .

The obtained values for fracture density of the method described above are higher than generally seen in for example fieldwork studies (Singhal & Gupta, 2010), because of the



scale difference and the much higher level of detail available in the  $\mu$ CT scans. The results on the  $\mu$ CT scans can therefore best be used for relative comparisons between samples.

**3.1.3.4. Fracture orientation:** Knowing the orientation of fractures in a dataset can be a very useful input in reservoir evaluation, especially if small-scale fractures display similar behaviour as the larger-scale network. In our case, due to the age of the wellbores, well orientation information is unfortunately not available for comparison to the datasets. Fracture orientation information thus lacks a proper reference frame here, but we do present a suitable routine. For the voxel-based data of complex fracture networks discretising the fractures is virtually impossible, hence orientation information cannot be obtained from distinct fractures. We instead use the concepts of the Hessian based filtering and segmentation method described in Section 3.1.2, but now use the eigenvector information rather than only eigenvalues. To reduce any effects of noise, the Hessian calculation is reapplied on the segmented data. The extracted eigenvector belonging to the largest Hessian eigenvalue represents the normal direction to the extracted fracture plane, at each voxel. These normal orientations are plotted and contoured in MATLAB, using density contouring relative to a Kalsbeek grid. Since this is a voxel-based approach, orientations of larger fractures (i.e. fractures containing more voxels) are automatically assigned more weight in the final stereographic projection. The density contouring of each stereographic projection is normalised to a single relative maximum value suitable for all samples, to allow comparison.

### 3.2. Thin sections

The limited resolution of  $\mu$ CT on plug-sized samples as shown in this study necessitates the use of better resolution methodologies to gain a better understanding of for example matrix porosity, cement contents, dolomite texture, et cetera. One option would be to create small subsamples from the original plugs and scan these at a better resolution using  $\mu$ CT or synchrotron X-ray CT. We however decided to create 2D thin sections after plug scanning, as this is a relatively cheaper and simpler method to apply, that still provides sufficient details, especially compared to the  $\mu$ CT data. For this comparison, we stitched thin section overviews from Scanning Electron Microscopy (SEM) images with back-scattered electrons (BSE) contrast. As a stitching routine, we either used the automatic Microsoft Research Image Composite Editor (ICE; Microsoft Research, 2011) or a self-written stitching script in FIJI. This stitching script reduces contrast and brightness variations introduced by the SEM (by dividing each image with its median filtered one with a kernel of 50 pixels), crops the images to remove warped and blurred edge areas, and combines (stitching by linear translation only) these into a single image for a thin section.

Figure 4 shows a comparison between  $\mu$ CT and SEM-BSE data, for an approximately matched 2D view from the 3D  $\mu$ CT data and a 2D thin section, in which the difference in resolution is clear. Especially the fine porosity in the matrix is not resolvable using the  $\mu$ CT resolution only. A segmentation of the SEM-BSE thin section overview was obtained using the automated binary segmentation by the Otsu threshold (Otsu, 1979) (example in Figure 5). The Otsu threshold – although still not ideal – provides good, repeatable results for the samples, due to the similar image acquisition and processing technique for the different samples in this study. It therefore allows us to readily compare the results on the samples.

Fracture aperture and density can potentially be determined on thin sections, but because of the higher level of detail visible (e.g. micropores) compared to  $\mu$ CT, bulk comparisons (e.g. aperture distribution) are not possible. Manual inspection on (approximately) matched  $\mu$ CT and thin section data – for example as in Figure 4 – however reveals that fracture apertures from  $\mu$ CT are often larger than from thin sections. This is most severe for narrow features that can still be recognised in the  $\mu$ CT data, due to the partial volume effect and blurring, whereas the difference gets small for relatively wide or open features. This resolution difference also affects the aperture variations detectable along a single fracture between  $\mu$ CT and thin sections (i.e. these variations can be observed in less detail in the  $\mu$ CT data).

## 4. Permeability experiments

As stated in the introduction, the methods described in Section 3 provide detailed information, but all apply to atmospheric conditions. To obtain a better link to the behaviour of the rocks at depth (i.e. more realistic reservoir conditions) we applied single phase steady state flow experiments under confining pressure, under the assumption that Darcy's law was valid. Either gas or water was used as pore fluid at room temperature, in two different experimental setups.

### 4.1. Gas permeability

Gas permeability experiments under confining pressure were carried out on 2 cm diameter plug samples at the École et Observatoire des Sciences de la Terre at the University of Strasbourg, France, using distilled water as the confining medium, and nitrogen gas as the pore fluid. A sketch of the experimental setup can be found in Heap et al. (2014). The permeability is determined using Darcy's law for a compressible gas (Scheidegger, 1974; Tanikawa & Shimamoto, 2006):

$$\kappa_{app} = \frac{\mu dx}{A} Q \frac{2P_{down}}{(P_{up})^2 - (P_{down})^2} \quad (\text{Equation 4.1})$$

Where  $\kappa_{app}$  is the apparent permeability [ $\text{m}^2$ ],  $\mu$  the dynamic viscosity of the pore fluid [Pa s],  $dx$  the sample length [m],  $A$  the cross sectional area to flow [ $\text{m}^2$ ],  $Q$  the flow rate [ $\text{m}^3/\text{s}$ ],  $P_{down}$  the downstream pore pressure [Pa] and  $P_{up}$  the upstream pore pressure [Pa]. During the experiments,  $P_{down}$  was kept constant at atmospheric pressure (0.1 MPa),  $P_{up}$  was varied in steps up to a maximum of 0.5 MPa, and the response in  $Q$  was measured. To compensate for the effect of gas slippage, the Klinkenberg correction is carried out (Klinkenberg, 1941) to obtain intrinsic permeability  $\kappa$ . For permeabilities above  $1 \cdot 10^{-15} \text{ m}^2$  the Forchheimer correction (Forchheimer, 1901) is carried out instead. With low pore fluid pressures compared to confining pressures, the confining pressure is set to represent effective confining pressure.

For the 3 cm diameter plug samples, gas permeability experiments could not be carried out in the above setup. However, nitrogen gas permeability measurements (under atmospheric conditions only) were done at OMV LEP, before  $\mu$ CT scanning, without Klinkenberg or

Forchheimer correction. This means a possible error on these measurements of 25% should be assumed.

## 4.2. Water permeability

Several 3 cm plug samples of this study were used in water permeability experiments under confining pressure at the Faculty of Civil Engineering and Geosciences at the Delft University of Technology, The Netherlands. Unfortunately, one of the fractured samples (Prottes TS1) disintegrated after  $\mu$ CT scanning and could not be used anymore for flow experiments, and was therefore replaced by a different fractured sample (Schönkirchen T32-430).

The experimental setup is similar to the gas permeability setup, but the axial pressure is controlled separately from the radial pressure. Tap water serves as pore fluid, and an incompressible oil (Multitherm PG-1<sup>®</sup>) was used as a confining medium. The permeability is determined using the linear form of Darcy's law (Tanikawa & Shimamoto, 2006):

$$\kappa = \frac{\mu dx}{A} \frac{Q}{DP} \quad (\text{Equation 4.2})$$

$Q$  was controlled and varied in steps, and  $DP$  (differential pore pressure in Pa, so the difference between  $p_{up}$  and  $p_{down}$ ) was measured by a sensitive differential pressure meter, with measurements at different  $Q$  (generally 4) combined in a single permeability value at one confining pressure.

Some tests show the response of permeability to several parameters, namely to axial pressure only, radial pressure only, the inversion of flow and time-dependency without flow. These results are shown in Figure 6. The fractured sample responds significantly more to changes in radial pressure (Figure 6a and b), and the value for radial pressure in all measurement series is therefore taken as the actual confining pressure. However, axial pressure was always kept as close as possible. Furthermore, inverting the flow (Figure 6c) does not have a significant effect on the permeability. If for example particle blockage is the main cause of permeability reduction in a sample, one would expect a short rise in permeability after flow inversion (e.g. Engler, 2010). Finally, a test of keeping the sample pressurised (Figure 6d) for several hours without flow shows no or only minor time-dependent effects are acting in the samples. These tests (Figure 6) thus indicate that the increasing confining pressure is the dominant mechanism for water permeability reduction shown in the following sections.

## 5. Results and discussion

The main results of this study are shown in Figure 7. Four examples of  $\mu$ CT scans (on 3 cm diameter plug samples) are shown (Figure 7b), portraying the differences in structure when moving from fractured host rock in the damage zone (1st and leftmost column), via a mixture of fractures and breccia (2nd column) and mosaic breccias (3rd column), towards cataclasites in the fault core (4th and rightmost column), as well as variations within the

samples themselves (for example, locally enhanced clay content in the matrix, or discontinuous vein fillings). When taking the MSHFF segmentation into account (Figure 7c), the differences between the porous fracture networks (and separate fractures) in different parts of the fault zone become even clearer. Note that apparent mismatches with the input data (Figure 7b) are mostly due to the contrast and brightness settings required to display the input data properly here. The following sections will discuss the different extracted parameters in more detail. The used samples and symbols are listed in Table 1 and 2.

### 5.1. Porosity

The results of porosity determination by laboratory methods (helium porosimetry for the 3 cm diameter samples, water saturation porosimetry for the 2 cm diameter samples),  $\mu$ CT and thin section analysis are shown in Figure 7d and listed in Table 2. Thin sections have not been made for all the available samples in Tables 1 and 2, and are thus not shown for every sample.

The trend in the porosity comparison is that the  $\mu$ CT results show the lowest porosity, followed by the laboratory results, and finally the thin section results. First of all, the  $\mu$ CT results show the porosity in the fracture network and pores with dimensions larger than the limited resolution of  $\mu$ CT ( $(12.5-20 \mu\text{m})^3 / \text{voxel}$ ), and are likely to be the main contributors to permeability in the samples. This has been confirmed – except for the cataclasite samples – by a connected cluster analysis on the data). Second, the lab porosity displays higher values than the  $\mu$ CT results. The main reason is that smaller porous structures than imaged with  $\mu$ CT can be reached with these laboratory techniques, even though only connected porosity is recorded. A theoretical non-connected porosity can be estimated from measured dry mass compared to assuming pure dolomite for the sample dimensions, resulting in a connected/non-connected porosity ratio of 0.6-0.95 (4 samples). Third and finally, the thin section SEM-BSE results show the porosity down to a much better resolution (imaging resolutions between  $(1.1 \mu\text{m})^2$  and  $(1.7 \mu\text{m})^2$  per pixel) than for  $\mu$ CT. Note that only full stitched overviews of thin sections have been taken (i.e. using the largest possible surface area for the porosity determination), and results on multiple thin sections on a sample are averaged. Also non-accessible (i.e. non-connected) porosity is included in these values, giving the highest relative porosity for thin sections. The connected/non-connected porosity fractions appear to match the theoretical values from the lab measurements. Caution should be taken in the comparison of thin section porosity due to possible sample alteration and damage (in preparation), and the limited 2D area compared to 3D volumes. Still, using thin sections (or any other imaging technique at a better resolution than full plug  $\mu$ CT) is required to obtain a more complete view of the structure of the samples.

### 5.2. Aperture

For aperture distributions, comparing the different samples is of main interest, and therefore shown in the separate Figure 8. In literature, aperture distributions derived from different methodologies (e.g. CT, optical profiling, numerical modelling), are often log-normal (e.g. Keller, 1998; Montemagno & Pyrak-Nolte, 1999; Karpyn et al., 2007; Sahimi, 2011). A (skewed) log-normal or exponential decay curve may be suitable interpretations for the data

in Figure 8, but the limited resolution of  $\mu$ CT for small apertures makes it difficult to confirm a single distribution curve.

Sample Schönkirchen T91-5p, which is a mixture between a mosaic breccia and pervasive fractures, differs from the other samples in aperture (Figure 8), as this sample has the largest open pores of all samples of this study. The other samples are relatively similar to each other, although the 2 cm diameter plug samples (open symbols) have consistently smaller aperture distributions than the 3 cm diameter samples (closed symbols). This is interpreted as an effect of  $\mu$ CT resolution and blurring. Real sample apertures may thus be somewhat lower, emphasising an important drawback of using aperture information from  $\mu$ CT. It is therefore recommended to use similar sample sizes throughout a comparing study, or – if computationally possible on the dataset – use calibrated routine that takes  $\mu$ CT blurring into account (e.g. Ketcham et al., 2010; Ketcham & Hildebrandt, 2014). For the data presented here, the recorded local aperture results in the 3D image data (e.g. Figure 3) may prove to be more useful than the bulk aperture distributions per sample (Figure 8), e.g. in permeability modelling.

### 5.3. Fracture density

The  $\mu$ CT fracture density values (Figure 7e) derived from aperture and porosity provide an independent parameter to characterise the rocks – possibly also in an automated way. Some correlation exists to the  $\mu$ CT porosity results, but it should be noted that this correlation is not constant for the different samples (i.e. fracture density/ $\mu$ CT porosity constant or related; see Table 2). For example for samples with mainly thin fractures (recorded by the local thickness aperture distribution), the fracture density relative to porosity is higher than for other samples. For exploration purposes, the fracture density can be an important parameter, especially when implemented into a model, combined with several of the other parameters derived in this study. However, as for these other parameters, it is better to only use similarly sized samples in such a comparison.

### 5.4. Fracture orientation

Some examples of the fracture orientation distribution are shown in Figure 7f, normalised to the same colour scheme. As a general trend, some clear and distinct fracture orientations are visible for the samples that are only fractured, the furthest away from the fault core. For the brecciated samples, the orientations are more spread out and of lower intensity than for the fractured samples. Finally, for the cataclasites, the fracture orientations that could be extracted show a large spread and no or only a very weak dominant orientation, as expected.

The results from the orientation determination can be used in (automated) classification schemes when applied on multiple samples, and can be compared to orientation data from other sources, if available.

### 5.5. Potential other parameters from imaging data

Several other parameters would be interesting to extract from  $\mu$ CT datasets, but attempts for the samples shown in this study were unfortunately not successful. For completeness and possible application in other studies, we mention them here briefly. First of all, fracture

spacing and fracture length are important parameters in for example Discrete Fracture Network modelling, but require separated fractures to obtain reasonable estimates. We attempted a filtering by fracture orientation (using the orientation data of Section 5.4), but this was not successful in automatically extracting separate fractures. Second, fracture roughness and self-similarity or self-affinity of fractures and fracture networks can be of interest for flow models.  $\mu$ CT data can potentially provide this information, but the limited resolution and sample size make these analyses (e.g. fracture profile extraction and box counting fractal analysis) inadequate on these data. For fracture roughness, better resolution data or specialised techniques such as optical profiling (2D or 3D) are recommended. For box counting, data covering a larger range of scales should be used as input data.

## 5.6. Permeability experiments

**5.6.1. Loading only**—Figure 7g shows the results from the gas and water permeability experiments under confining pressure. For the 3 cm diameter plugs, the available gas permeability experiments without confining pressure (and without correction, so a 25% error margin should be assumed) are shown as black stars for comparison. There is no simple porosity-permeability relationship that could cover all samples (Figure 9).

When comparing the results in Figure 7g, first, the various breccias (middle two columns in the figure) show the highest initial and remaining permeabilities with increasing confining pressure. This can be explained by the complex variations in fracture orientation and apertures, preventing the open porosity structure to close efficiently. Second, the samples belonging to the damage zone with predominately fractures (left column in Figure 7g) show somewhat lower permeabilities, and relatively the largest decrease in permeability with confining pressure. The simpler geometry of the fractures probably makes closing more efficient than for breccias. Third and finally, the cataclasite samples (right column in Figure 7g) show the lowest permeabilities, with different behaviour for the gas and water experiments. The gas permeability experiments show an initial drop, followed by virtually no change in permeability, attributed to the varying fracture orientations and the overall low porosity in the sample. For the water permeability experiment however, a more severe drop is observed. Although this may be true behaviour, there is a chance that at these low permeability values, some non-steady state flow effects were still acting during the experiment, or that the sample has been altered due to sample preparation. The results of the water permeability experiment on this cataclasite sample are thus the least convincing of all experiments.

There is no clear trend in the difference between the gas and water permeability experiments on similar samples. Gas permeability measurements have been reported to lead to higher permeability values than water permeability experiments (e.g. Tanikawa & Shimamoto (2006) and Faulkner & Rutter (2000), on different rock types). However, there is no way to distinguish this from heterogeneity between samples, without performing experiments with both pore fluids on exactly the same sample. Furthermore, the gas permeability experiments without confining pressure (black stars, non- corrected) also show no clear trend compared to the water permeability experiments on the same samples. Measured permeabilities can

thus definitely not be considered as a single true value for permeability, especially not per fracture class type.

When taking all experiments together, the general trend is that most of the permeability drop in these samples occurs before reaching 20 MPa, which is best visible for the gas permeability experiments because of the longer confining pressure range in the experiments. Most likely, these initial drops in permeability represent a fast closing of open pores/fractures, until asperities prevent further closing. Probably, also some elastic effects are at play in the samples, and some interesting observations can be made about these processes when also looking at unloading and reloading of samples (Section 5.6.2).

Because the actual fluid pressures in the reservoirs are not available, converting the effective confining pressures in the experiments to actual reservoir depths is not straightforward. However, taking the depths of sample origin and by assuming the reservoirs are not in overpressure, the reservoirs are most likely at pressures above the range with the main permeability drop in the samples (i.e. >20 MPa). In future studies, if the stress field in the reservoir is known, it may prove to be more useful to apply a proxy to such a stress field rather than an isotropic confining pressure as applied in this study.

**5.6.2. Loading and unloading**—The permeability response to the loading path (for confining pressure) was investigated in the water permeability experiments setup (for fractured sample Schönkirchen T32-430; Figure 10). Clearly, the order of loading and unloading steps has an effect on the measured permeability values. Following an exponential decay curve, one could argue that continuous loading beyond the maximum intermediate confining pressure (point 4) would lead to results such as shown by arrow a in the figure. In a similar manner, one could argue that with only immediate unloading after maximum confining pressure, behaviour such as for arrow b could be expected. The actual loading and unloading path however results in a lower permeability than for the arrows.

The dependence on the actual loading- and unloading path has been observed often, in various rock types (e.g. Faulkner & Rutter, 2000; Selvadurai & Glowacki, 2008). Here, confining pressure does not have to exceed the intermediate maximum pressure before extra permeability reduction can occur, as observed by Selvadurai & Glowacki (2008). Cycling of loading and unloading until no path-dependent behaviour is visible anymore – such as in Faulkner & Rutter (2000) – would be an experimental possibility. Since the samples were however unloaded during uplift, we do not think a minimum permeability measurement after cyclic loading and unloading is likely to be a better representation of actual reservoir permeability conditions than the path-dependent measurements we did perform.

Several reasons could cause the path-dependent behaviour we see in these experiments. For example, consecutive partial destruction of weak asperities or small shear movements along cracks may be acting, and also residual other fluid phases might play a role. Permeability reduction by particle blockage seems unlikely as this effect did not come out of our flow direction inversion experiments (Figure 6c). More experiments would thus be necessary to determine the mechanisms at play. Measuring the same loading and unloading path on all samples would be a good approach, although this requires more experiment time. The

experiments may also be tailored to certain reservoir depths or conditions. However, since these experiments show that loading and unloading cannot be simply inverted (but in fact show hysteresis-like behaviour), even permeability determined at maximum loading after several stages of loading and unloading may not reflect actual reservoir conditions well. Obtaining the real permeability under original reservoir conditions may therefore not be possible from core samples, but similar measurements between samples should be comparable in a relative sense.

**5.6.3.  $\mu$ CT after permeability experiments**—For a single sample (Prottes TS1-4p), a  $\mu$ CT scan was made before and after a water permeability experiment under confining pressure, and registered (matched) in 3D (Figure 11). Contrary to the  $\mu$ CT scans shown before, these scans were made at the Faculty of Civil Engineering and Geosciences at the Delft University of Technology, The Netherlands, using a Phoenix Nanotom  $\mu$ CT, and reconstructed with a resolution of  $(15 \mu\text{m})^3$  per voxel. When overlaying the two datasets, virtually no difference can be observed. Only a few small differences are visible at the planar edges of the sample (not shown in Figure 11), but these are most likely related to sample handling after the permeability experiments. These  $\mu$ CT results show that the changes in the sample (as recorded in the permeability curve in Figure 11f) are not captured by the resolution of the  $\mu$ CT scan. This means, the permeability reduction may occur by small aperture reductions or changes in pores which are not observable by  $\mu$ CT. A technique with a much better resolution would thus be necessary to capture these differences, or a more complex approach can be taken – if available – such as CT scanning during compression and flow (e.g. Watanabe et al., 2011).

## 5.7. Permeability models

The permeability results from laboratory experiments should ideally be connected to permeability determined from the imaging results. Here, we investigate the use of a statistical method defined by Gueguen and Dienes (1989), where a model of cylindrical 2D cracks is proposed, which is expressed as follows in an isotropic case:

$$\kappa = \frac{4\pi}{15} f \frac{\bar{w}^3 \bar{c}^2}{\bar{l}^3} \quad (\text{Equation 5.1})$$

$f$  is a factor between 0 and 1 depicting the fraction of connected fractures.  $\bar{w}$  is the average half-crack aperture,  $\bar{c}$  the average crack radius and  $\bar{l}$  the average crack spacing. Using a definition for porosity in the crack model, the following can be derived from Equation 5.1 (Gueguen and Dienes (1989):

$$\kappa = \frac{2}{15} f \bar{w}^2 \bar{\Phi} \quad (\text{Equation 5.2})$$

where  $\bar{\Phi}$  is the porosity fraction. Taking the geometric mean of the aperture,  $f=1$  and the porosity from different methods (Table 2), the results of the model permeability are very



different relative to the measured permeability values, with overestimations of a factor ( $\kappa_{model}/\kappa_{measured}$ ) in the order of magnitude of  $10^3$ - $10^5$ . Even when taking a lower value for  $f$ , a lower geometric mean for the aperture (compensating for the possible overestimation of aperture), and the lowest possible porosity values, the overestimation of permeability by this model stays significant. Among the other reasons this particular model may not work are a) the models assume isotropy for simplicity, and this is not likely for these samples; b) the variables in the model are statistically independent, whereas here, we observe larger apertures for larger fractures and c) in the model, connectivity is assumed to be by cracks only, but these samples are likely to have significant matrix connectivity.

We therefore argue that to obtain more realistic values for permeability from  $\mu$ CT data, more complex models than in Equation 5.2 should be applied, or better, numerical simulations by for example Finite Element Modelling (e.g. Hoyer et al., 2012) or a Lattice Boltzmann approach (e.g. Degruyter et al., 2010) that use the actual geometry from the image data.

## 5.8. Synthesis and recommendations

In the previous sections, the results for various parameters from several methodologies have been shown and discussed in detail. On  $\mu$ CT data of a small set of 7 differently fractured dolomite samples, we have been able to extract bulk values and distributions for porosity, fracture aperture, fracture density and fracture orientation, while also being able to look at the local distribution of these parameters, and the relationships between them. A disadvantage is that the voxel-based and bulk parameters approach taken does not allow for efficient separation into single fractures, making analyses on e.g. fracture spacing and roughness not feasible. An advantage of the chosen methodology is however that fairly little manual interpretation and -processing is required, making the shown bulk and voxel-based analyses suitable for an automation routine, which could be applied in extended studies. Another option would be to combine an extended  $\mu$ CT study with a fieldwork study on a reservoir analogue, to improve both the results obtainable by  $\mu$ CT as well as the fieldwork interpretations. The investments required for a large  $\mu$ CT study should however be kept in mind; i.e. it has to be possible to obtain important information that cannot be derived using other, less demanding techniques, or it should be possible to confirm (or disprove) or calibrate the outcome from different techniques by using the  $\mu$ CT results.

The influence of small variations and heterogeneities in the samples shows that no single sample can be considered representative for a large area, also meaning that the samples used for  $\mu$ CT scanning do clearly not serve as a Representative Elementary Volume (REV). A related limitation on the REV is due to the sampling itself, since we can only use samples that do not disintegrate upon plug creation. On the other end of the scale, also small features are not included with respect to the resolution limits of  $\mu$ CT, again limiting the possibilities of obtaining an REV with  $\mu$ CT only. To overcome these problems with REV, for example datasets of adjacent samples could be combined, or links to data at a different scale could be used. Such approaches for upscaling may be successful, but most likely require additional modelling on the data.

## 6. Conclusion

The main question we tried to answer in this paper was how to efficiently analyse natural fracture networks in dense rocks. We have shown that 3D  $\mu$ CT imaging is possible on small (2 to 3 cm diameter) plug samples of narrowly fractured dolomites, and that this image data can be successfully processed using the MSHFF routine. Using this processed data, the internal fracture and pore structure of the samples can be visualised, and parameters such as porosity, fracture aperture, fracture density and fracture orientation can be extracted.  $\mu$ CT has important limitations (mainly on sample size and resolution), and can therefore not serve as a complete replacement for other analysis techniques. It can however serve as a valuable extra source of information, especially when applied on larger sets of data. As an addition to  $\mu$ CT imaging, we obtained thin section data for more detailed analyses on the samples, as well as to obtain an additional measure for porosity. Finally, permeability measurements on the samples under confining pressure provide insights on the flow behaviour of the samples at depth, but also show that such measurements can only provide an approximation for the natural situation.

When combining the results on the samples shown in this study with a fault zone interpretation from damage zone to fault core, the differences between the samples become clear. Small variations in microstructure can have a large influence on the observable parameters. Fractured samples (the furthest away from the fault core) generally have intermediate observed porosity and permeability, and clear distinct fracture orientations. Brecciated samples (from closer to the fault core) have the highest porosities and permeabilities, and a wider spread in fracture orientations. Their fracture densities are high. Finally, cataclasite samples have the lowest porosities and permeabilities, low fracture densities and no fracture orientation preference. The analysis steps taken and the results shown here can be used in more extensive studies, and show that (partial) automation of sample analysis is possible. Moreover, results as the ones shown in this study can serve as input for modelling and simulations, where especially the obtained 3D information and the flow behaviour at depth are important parameters that may be difficult to characterise using other methods.

## Acknowledgements

The study was funded by the OMV and the Austrian Science Fund, Austria (FWF): [V151-N22]. The authors would like to thank the OMV for providing the samples presented in this paper. Permeability experiments in Strasbourg were conducted in the ÖAD WTZ (Amadée programme) project FR 05/2014. We would also like to thank Christian Gusenbauer (FHOÖ, Wels, Austria) for performing the main  $\mu$ CT scans and reconstructions, as well as Jan Etienne and Wim Verwaal (Delft University of Technology, The Netherlands) for their great technical support. Furthermore, we would like to thank Theresa Schröckenfuchs and Helene Bauer (University of Vienna, Austria) for their help with the fault zone interpretation and diagrams based on their fieldwork studies. Finally, we wish to thank three anonymous reviewers for their comments and suggestions that helped in improving this paper.

## References

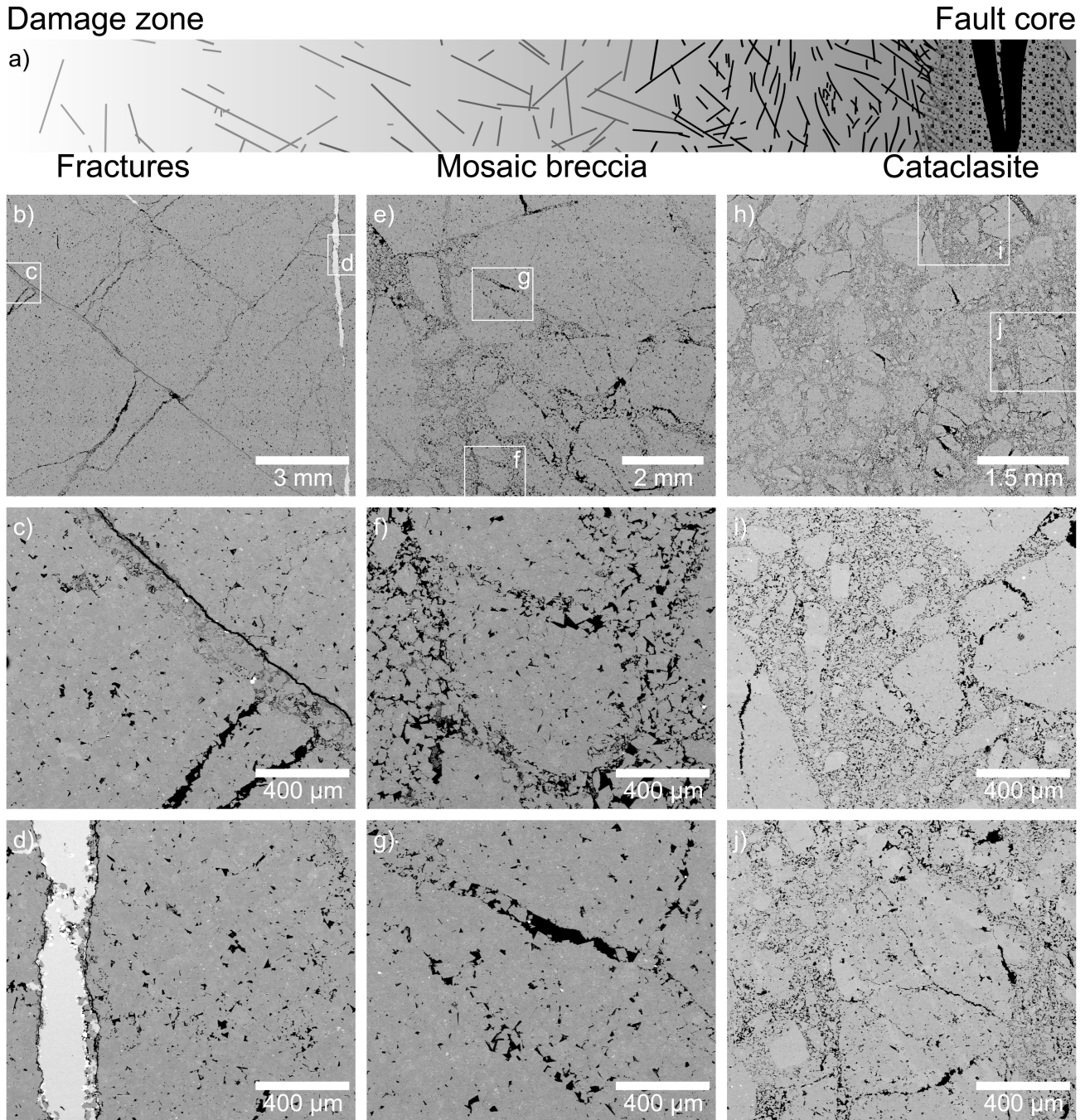
- Aguilera, R. Naturally Fractured Reservoirs. 2. PennWell Books; Tulsa: 1995.
- Andersen MA, Duncan B, McLin R. Core truth in formation evaluation. *Oilfield Review*. 2013; 2013(2):16–25.
- Anselmetti FS, Luthi S, Eberli GP. Quantitative characterization of carbonate pore systems by digital image analysis. *AAPG Bulletin*. 1998; 82(10):1815–1836.

- Antonellini M, Mollema PN. A natural analog for a fractured and faulted reservoir in dolomite: Triassic Sella group, Northern Italy. *AAPG Bulletin*. 2000; 84(3):314–344.
- API. Recommended practices for core analysis. 2. American Petroleum Institute; 1998. p. 236 Recommended Practice 40
- Arzmüller, G.; Buchta, S.; Ralbovský, E.; Wessely, G. The Vienna Basin. In: Golonka, J.; Picha, FJ., editors. *The Carpatians and their foreland: Geology and hydrocarbon resources*. AAPG Memoir. Vol. 84. 2006. p. 191-204.
- Barnhoorn A, Cox SF, Robinson DJ, Senden T. Stress- and fluid-driven failure during fracture array growth: implications for coupled deformation and fluid flow in the crust. *Geology*. 2010; 38(9):779–782. doi: 10.1130/G31010.1.
- Bauer, H. *Deformationsprozesse und hydrogeologische Eigenschaften von Störungszonen in Karbonatgesteinen*. Earth Sciences, University of Vienna; Austria: 2010. p. 102M.Sc Dissertation
- Bertels SP, DiCarlo DA, Blunt MJ. Measurement of aperture distribution, capillary pressure, relative permeability, and in situ saturation in a rock fracture using computed tomography scanning. *Water Resources Research*. 2001; 37(3):649–662.
- Billi A. Microtectonics of low-P low-T carbonate fault rocks. *Journal of Structural Geology*. 2010; 32:1392–1402.
- Billi A, Salvini F, Storti F. The damage zone-fault core transition in carbonate rocks: implications for fault growth, structure and permeability. *Journal of Structural Geology*. 2003; 25:1779–1794.
- Blendinger W. Dolomitization of the Dolomites (Triassic, Northern Italy): Pilot study. *Neues Jahrbuch für Geologie und Paläontologie-Abhandlungen*. 1997; 204(1):83–110.
- Bossie-Codreanu D, Wolf K-HAA, Ephraim R. A new characterization method for coal bed methane. *Geologica Belgica*. 2004; 7(3-4):137–145.
- Christe, PG. *Geological Characterization of Cataclastic Rock Samples Using Medical X-ray Computerized Tomography: Towards a Better Geotechnical Description*. Faculté Environnement Naturel, Architectural et Construit. École Polytechnique Fédérale de Lausanne (EPFL); Lausanne: 2009. p. 338Ph.D. Dissertation
- Cnudde V, Masschaele B, Dierick M, Vlassenbroeck J, Hoorebeke L, Jacobs P. Recent progress in X-ray CT as a geosciences tool. *Applied Geochemistry*. 2006; 21(5):826–832. doi:10.1016/j.apgeochem.2006.02.010.
- Degruyter W, Burgisser A, Bachmann O, Malaspina O. Synchrotron X-ray microtomography and lattice Boltzmann simulations of gas flow through volcanic pumices. *Geosphere*. 2010; 6(5):470–481.
- Dougherty, RP.; Kunzelmann, K-H. Computing Local Thickness of 3D Structures with ImageJ. *Microscopy & Microanalysis Meeting*; Ft. Lauderdale, Florida. August 2007; 2007. Conference Presentation. <http://www.optinav.com/LocalThicknessEd.pdf>
- Ehrig, K.; Goebbels, J.; Meinel, D.; Paetsch, O.; Prohaska, S.; Zobel, V. Comparison of Crack Detection Methods for Analyzing Damage Processes in Concrete with Computed Tomography. *Proceedings International Symposium on Digital Industrial Radiology and Computed Tomography (DIR)*; Berlin, Germany. 2011; 2011. p. 8
- Ekstrom MP, Dahan CA, Chen MY, Lloyd PM, Rossi DJ. Formation imaging with microelectrical scanning arrays. *The Log Analyst*. May-Jun;1987 :294–306. 1987.
- Ellis, BR. *Geologic carbon sequestration in deep saline aquifers: brine acidification and geochemical alterations of reactive leakage pathways*. Faculty of Princeton University, Department of Civil and Environmental Engineering; Princeton: 2012. p. 118Ph.D. Dissertation
- Engler, TW. [Accessed 22 May 2014] Fluid flow in porous media. *Petroleum Engineering 524 Lecture Notes*, New Mexico Tech. 2010. <http://infohost.nmt.edu/~petro/faculty/Engler524/>
- Faulkner DR, Rutter EH. Comparisons of water and argon permeability in natural clay-bearing fault gouge under high pressure at 20°C. *Journal of Geophysical Research*. 2000; 105(B7):16415–16426.
- Flügel, E. *Microfacies of Carbonate Rocks: Analysis, Interpretation and Application*. Springer; Berlin, Heidelberg, New York: 2004.
- Forchheimer P. *Wasserbewegung durch Boden*. *Zeitschrift des Vereines deutscher Ingenieure*. 1901; 45:1782–1788.

- Frangi, AF.; Niessen, WJ.; Vincken, KL.; Viergever, MA. Multiscale Vessel Enhancement Filtering. In: Wells, WM.; Colchester, A.; Delp, SL., editors. Proceedings Medical Image Computing and Computer-Assisted Intervention (MICCAI) 1998. Cambridge, Massachusetts, USA: 1998. p. 130-137. Lecture Notes in Computer Science 1496
- Fruth I, Scherreiks R. Hauptdolomit - Sedimentary and Paleogeographic Models (Norian, Northern Calcareous Alps). *Geologische Rundschau*. 1984; 73:305–319.
- Fusi N, Martinez-Martinez J. Mercury porosimetry as a tool for improving quality of micro-CT images in low porosity carbonate rocks. *Engineering Geology*. 2013; 166:272–282. doi:10.1016/j.enggeo.2013.10.002.
- Gale, JFW.; Laubach, SE.; Marrett, RA.; Olson, JE.; Holder, J.; Reed, RM. Predicting and characterizing fractures in dolostone reservoirs: using the link between diagenesis and fracturing. In: Braithwaite, CJR.; Rizzi, G.; Darke, G., editors. The geometry and petrogenesis of dolomite hydrocarbon reservoirs. 2004. p. 177-192. Geological Society of London, Special Publications 235 2004
- Gueguen Y, Dienes J. Transport properties of rocks from statistics and percolation. *Mathematical Geology*. 1989; 21(1):1–13.
- Hakami, E.; Einstein, HH.; Gentier, S.; Iwano, M. Characterisation of fracture apertures - Methods and Parameters. Proceedings of the Eighth International Congress on Rock Mechanics; Tokyo. September 1995; 1995. p. 751
- Heap MJ, Lavallée Y, Petrakova L, Baud P, Reuschlé T, Varley NR, Dingwell DB. Microstructural controls on the physical and mechanical properties of edifice-forming andesites at Volcán de Colima, Mexico. *Journal of Geophysical Research: Solid Earth*. 2014; 119(4):2925–2963. doi: 10.1002/2013JB010521.
- Hoyer, S.; Exner, U.; Voorn, M.; Rath, A. 3D Modeling of fracture flow in core samples using  $\mu$ -CT data. Proceedings COMSOL Conference; Milan, Italy. 2012; 2012. <http://www.comsol.com/offers/conference2012papers/papers/presentation/area/geophysics/id/13295/>
- Iassonov P, Tuller M. Application of Segmentation for Correction of Intensity Bias in X-Ray Computed Tomography Images. *Vadose Zone Journal*. 2010; 9(1):187–191. doi:10.2136/vzj2009.0042.
- Isakov E, Ogilvie SR, Taylor CW, Glover PWJ. Fluid flow through rough fractures in rocks I: high resolution aperture determinations. *Earth and Planetary Science Letters*. 2001; 191:267–282.
- Jia L, Chen M, Jin Y. 3D imaging of fractures in carbonate rocks using X-ray computed tomography technology. *Carbonates and Evaporites*. 2013; 29:147–153. doi: 10.1007/s13146-013-0179-9.
- Kaestner A, Lehmann E, Stampanoni M. Imaging and image processing in porous media research. *Advances in Water Resources*. 2008; 31:1174–1187. doi:10.1016/j.advwatres.2008.01.022.
- Karpyn ZT, Grader AS, Halleck PM. Visualization of fluid occupancy in a rough fracture using micro-tomography. *Journal of colloid and interface science*. 2007; 307(1):181–187. doi:10.1016/j.jcis.2006.10.082. [PubMed: 17140592]
- Keller A. High Resolution, Non-destructive Measurement and Characterization of Fracture Apertures. *International Journal of Rock Mechanics and Mining Sciences*. 1998; 35(8):1037–1050. doi: 10.1016/S0148-9062(98)00164-8.
- Ketcham R, Slotke DT, Sharp JMJ. Three-dimensional measurement of fractures in heterogeneous materials using high-resolution X-ray computed tomography. *Geosphere*. 2010; 6(5):499–514. doi: 10.1130/ges00552.1.
- Ketcham RA, Carlson WD. Acquisition, optimization and interpretation of X-ray computed tomographic imagery: applications to the geosciences. *Computers & Geosciences*. 2001; 27(4): 381–400. doi:10.1016/S0098-3004(00)00116-3.
- Ketcham RA, Hildebrandt J. Characterizing, measuring, and utilizing the resolution of CT imagery for improved quantification of fine-scale features. *Nuclear Instruments and Methods in Physics Research B*. 2014; 324:80–87.
- Klinkenberg, LJ. Drilling and Production Practices. American Petroleum Institute; 1941. The permeability of Porous media to liquids and gases; p. 200-213.

- Klobes P, Riesemeier H, Meyer K, Goebels J, Hellmuth K-H. Rock porosity determination by combination of X-ray computerized tomography with mercury porosimetry. *Fresenius' Journal of Analytical Chemistry*. 1997; 357(5):543–547.
- Kulatilake PHSW, Park J, Balasingam P, Morgan R. Quantification of aperture and relations between aperture, normal stress and fluid flow for natural single rock fractures. *Geotechnical and Geological Engineering*. 2008; 26:269–281. doi: 10.1007/s10706-007-9163-2.
- Landis EN, Nagy EN, Keane DT. Microstructure and fracture in three dimensions. *Engineering Fracture Mechanics*. 2003; 70(7-8):911–925. doi:10.1016/S0013-7944(02)00157-1.
- Lenoir N, Bornert M, Desrues J, Bésuelle P, Viggiani G. Volumetric digital image correlation applied to X-ray microtomography images from triaxial compression tests on argillaceous rock. *Strain*. 2007; 43:193–205.
- Masaryk P, Lintnerová O. Diagenesis and porosity of the Upper Triassic carbonates of the pre-neogene Vienna basin basement. *Geologica Carpathica*. 1997; 48:371–386.
- Mees, F.; Swennen, R.; Van Geet, M.; Jacobs, P., editors. *Applications of Computed Tomography in the Geosciences*. Geological Society; London: 2003. p. 250 Special Publications (215) ISBN: 1862391394
- Meijering, EHW. FeatureJ 1.6.0. Biomedical Imaging Group Rotterdam; Erasmus MC - University Medical Center Rotterdam; The Netherlands: 2010. 2002–2010. <http://www.imagescience.org/meijering/software/featurej/> [Accessed 22 May 2014]
- Meister P, McKenzie JA, Bernasconi SM, Brack P. Dolomite formation in the shallow seas of the Alpine Triassic. *Sedimentology*. 2013; 60:270–291. doi: 10.1111/sed.12001.
- Microsoft Research. [Accessed 22 May 2014] Image Composite Editor (ICE). v.1.4.42011. <http://research.microsoft.com/en-us/um/redmond/groups/ivm/ICE/>
- Montemagno CD, Pyrak-Nolte LJ. Fracture network versus single fractures: measurement of fracture geometry with X-ray tomography. *Physics and Chemistry of the Earth A*. 1999; 24(7):575–579.
- Muralidharan, V.; Chakravarthy, D.; Putra, E.; Schechter, DS. Investigating fracture aperture distributions under various stress conditions using X-ray CT scanner. 5th Canadian Petroleum Society International Petroleum Conference; Calgary, Alberta, Canada. 2004; 2004.
- Nelson, RA. *Geologic Analysis of Naturally Fractured Reservoirs*. 2. Gulf Professional Publishing; Boston, Oxford, Auckland, Johannesburg, Melbourne, New Delhi: 2001. ISBN: 0-88415-317-7
- Neuville A, Toussaint R, Schmittbuhl J, Koehn D, Schwarz J-O. Characterization of major discontinuities from borehole cores of the black consolidated marl formation of Draix (French Alps). *Hydrological Processes*. 2012; 26:2085–2094. doi: 10.1002/hyp.7984.
- Otsu N. A threshold selection method from gray-level histograms. *IEEE Transactions on systems, man and cybernetics, SMC*. 1979; 9(1):62–66.
- Peresson H, Decker K. The Tertiary dynamics of the northern Eastern Alps (Austria): changing palaeostresses in a collisional plate boundary. *Tectonophysics*. 1997; 272:125–157.
- Plouraboué F, Kurowski P, Hulin J-P, Roux S, Schmittbuhl J. Aperture of rough cracks. *Physical Review E*. 1995; 51(3):1675–1685.
- Prensky, SE. Advances in borehole imaging technology and applications. In: Lovell, MA.; Williamson, G.; Harvey, PK., editors. *Borehole imaging: applications and case histories*. 1999. p. 1-43. Geological Society of London, Special Publications 159 1999
- Sahimi, M. *Flow and transport in porous media and fractured rock: from classical methods to modern approaches*. 2. Wiley-VCH Verlag GmbH & Co. KGaA; Weinheim: 2011. ISBN: 978-3-527-40485-8
- Scheidegger, AE. *The physics of flow through porous media*. 3. University of Toronto Press; Toronto: 1974. p. 353
- Schindelin J, Arganda-Carreras I, Frise E, Kaynig V, Longair M, Pietzsch T, Preibisch S, Rueden C, Saalfeld S, Schmid B, Tinevez JY, White DJ, Hartenstein V, Eliceiri K, Tomancak P, Cardona A. Fiji: an open-source platform for biological-image analysis. *Nature methods*. 2012; 9(7):676–682. doi:10.1038/nmeth.2019. [PubMed: 22743772]
- Schröckenfuchs, T-C. *Mikrotektonische Analyse und Reservoireigenschaften von karbonatischen Störungsgesteinen*. University of Vienna; Austria: 2012. p. 111 M.Sc Dissertation, Earth Sciences

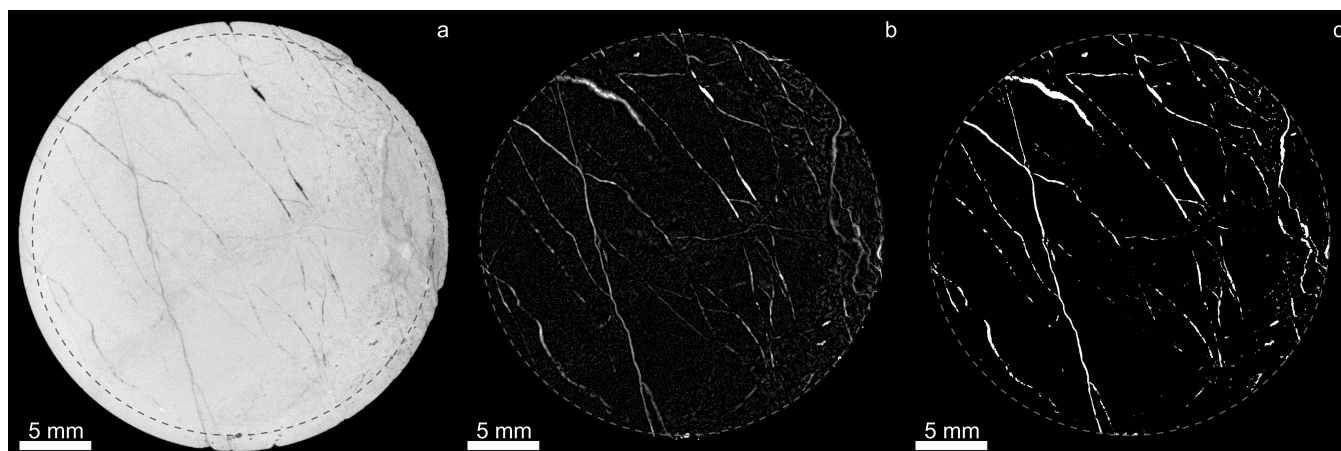
- Sellers, E.; Vervoort, A.; Van Cleynenbreugel, J. Three-dimensional visualization of fractures in rock test samples, simulating deep level mining excavations, using X-ray computed tomography. In: Mees, F.; Swennen, R.; Van Geet, M.; Jacobs, P., editors. *Applications of X-ray Computed Tomography in the Geosciences*. Geological Society; London: 2003. p. 69-80. Special Publications (215) doi:10.1144/GSL.SP.2003.215.01.07
- Selvadurai APS, Glowacki A. Permeability hysteresis of limestone during isotropic compression. *Groundwater*. 2008; 46(1):113–119. doi: 10.1111/j.1745-6584.2007.00390.x.
- Sezgin M, Sankur B. Survey over image thresholding techniques and quantitative performance evaluation. *Journal of Electronic Imaging*. 2004; 13(1):146–165. doi:10.1117/1.1631315.
- Sharifzadeh M, Mitani Y, Esaki T. Rock joint surfaces measurement and analysis of aperture distribution under different normal and shear loading using GIS. *Rock Mechanics and Rock Engineering*. 2008; 41(2):299–323. doi: 10.1007/s00603-006-0115-6.
- Sibley DF, Gregg JM. Classification of dolomite rock textures. *Journal of Sedimentary Petrology*. 1987; 57(6):967–975.
- Singhal , BBS.; Gupta , R,P. *Applied hydrogeology of fractured rocks*. 2. Springer Science+Business Media B.V.; Dordrecht, Heidelberg, London, New York: 2010. ISBN: 978-9048187890
- Tanikawa W, Shimamoto T. Klinkenberg effect for gas permeability and its comparison to water permeability for porous sedimentary rocks. *Hydrology and Earth System Sciences Discussions*. 2006; 3:1315–1338.
- The Mathworks, Inc.. MATLAB® R2011a. Natick, Massachusetts, USA: 2011. <http://www.mathworks.com/products/matlab/> [Accessed 22 May 2014]
- Van Geet M, Swennen R. Quantitative 3D-fracture Analysis by Means of Microfocus X-ray Computer Tomography ( $\mu$ CT): an example from coal. *Geophysical Research Letters*. 2001; 28(17):3333–3336. doi:10.1029/2001GL013247.
- Voorn M, Exner U, Rath A. Multiscale Hessian fracture filtering for the enhancement and segmentation of narrow fractures in 3D image data. *Computers and Geosciences*. 2013; 57:44–53.
- Watanabe N, Ishibashi T, Ohsaki Y, Tsuchiya Y, Tamagawa T, Hirano N, Okabe H, Tsuchiya N. X-ray CT based numerical analysis of fracture flow for core samples under various confining pressures. *Engineering Geology*. 2011; 123:338–346. doi:10.1016/j.enggeo.2011.09.010.
- Wennberg OP, Rennan L, Basquet R. Computed tomography scan imaging of natural open fractures in a porous rock; geometry and fluid flow. *Geophysical Prospecting*. 2009; 57:239–249. doi: 10.1111/j.1365-2478.2009.00784.x.
- Woodcock NH, Omma JE, Dickson JAD. Chaotic breccia along the Dent Fault, NW England: implosion or collapse of a fault void? *Journal of the Geological Society*. 2006; 163:431–446. doi: 10.1144/0016-764905-067.
- Yang Z, Peng X-F, Lee D-J, Chen M-Y. An Image-Based Method for Obtaining Pore-Size Distribution of Porous Media. *Environmental Science & Technology*. 2009; 43(9):3248–3253. [PubMed: 19534142]
- Zabler S, Rack A, Manke I, Thermann K, Tiedemann J, Harthill N, Riesemeier H. High-resolution tomography of cracks, voids and micro-structure in greywacke and limestone. *Journal of Structural Geology*. 2008; 30:876–887. doi:10.1016/j.jsg.2008.03.002.
- Zalewska, J.; Kaczmarczyk, J.; Lykowska, G. Use of X-ray computed microtomography for analysis of drill cores. *Nafta-Gaz, Instytut Nafta I Gazu - Polish Oil and Gas Natural Research Institute*; 2011.
- Zimmer, W.; Wessely, G. Exploration Results in Thrust and Subthrust Complexes in the Alps and Below the Vienna Basin in Austria. In: Wessely, G.; Liebl, W., editors. *Oil and Gas in Alpidic Thrustbelts and Basins of Central and Eastern Europe*. EAGE Special Publication; London: 1996. p. 81-107.



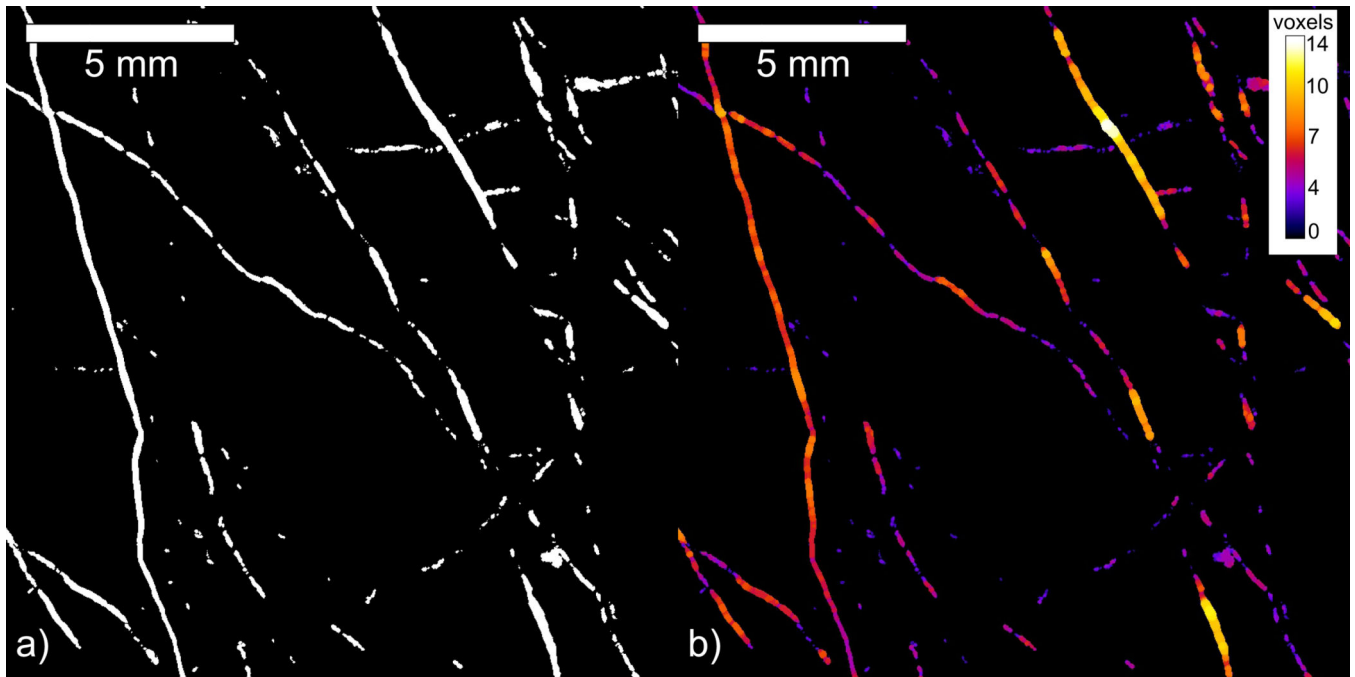
**Fig. 1.** Stretched SEM-BSE images (b, e and h) and corresponding detailed views showing representative microstructures of different fault rocks in a fault zone (a). b) Sample Prottes TS1-8sp interpreted as damage zone, with open fractures, fractures filled with clay and small dolomite fragments (c), and calcite veins with framboidal pyrite (brightest spots) (d). e) Brecciated sample Prottes TS1-3sp showing several dolomite host rock fragments embedded in finer material (f), or bordered by open fractures (g). h) Cataclasite sample Strasshof (i, j).

T4-2sp showing broken host-rock fragments in a fine-grained cataclastic matrix (i), sometimes preserving older vein structures within the fragments (j).

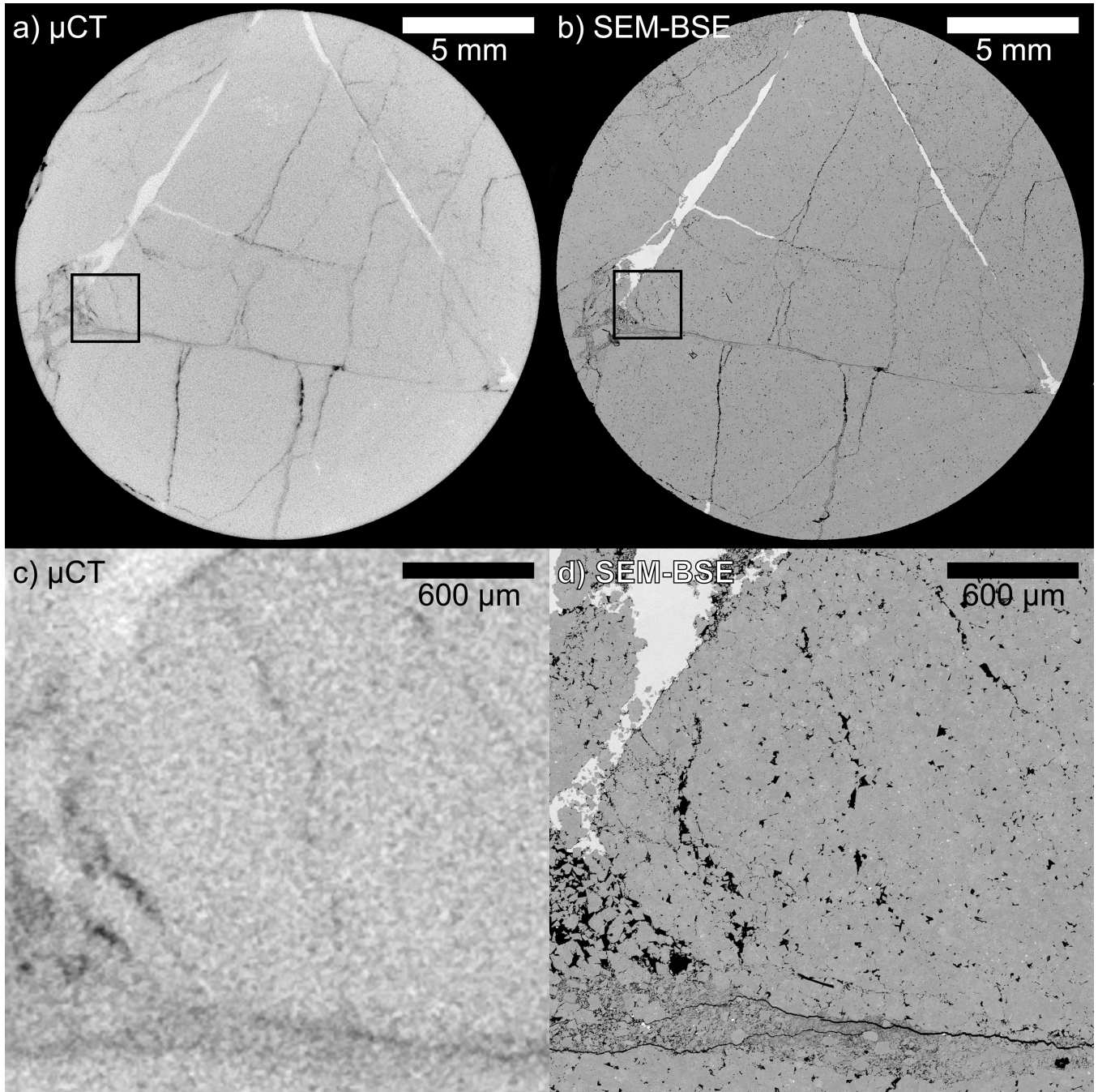




**Fig. 2.** 2D slice from a 3D  $\mu$ CT dataset on sample Prottes TS1 (reconstructed at  $(18.9 \mu\text{m})^3$  per voxel), demonstrating the filtering (b) and binary segmentation (c) routine applied here. The same example slice is used as in Voorn et al. (2013), but the combination of Gaussian analysis scales and the final segmentation are different. Brightness and contrast were adapted for (b) to allow display here. The final region of interest is indicated as a dashed circle.



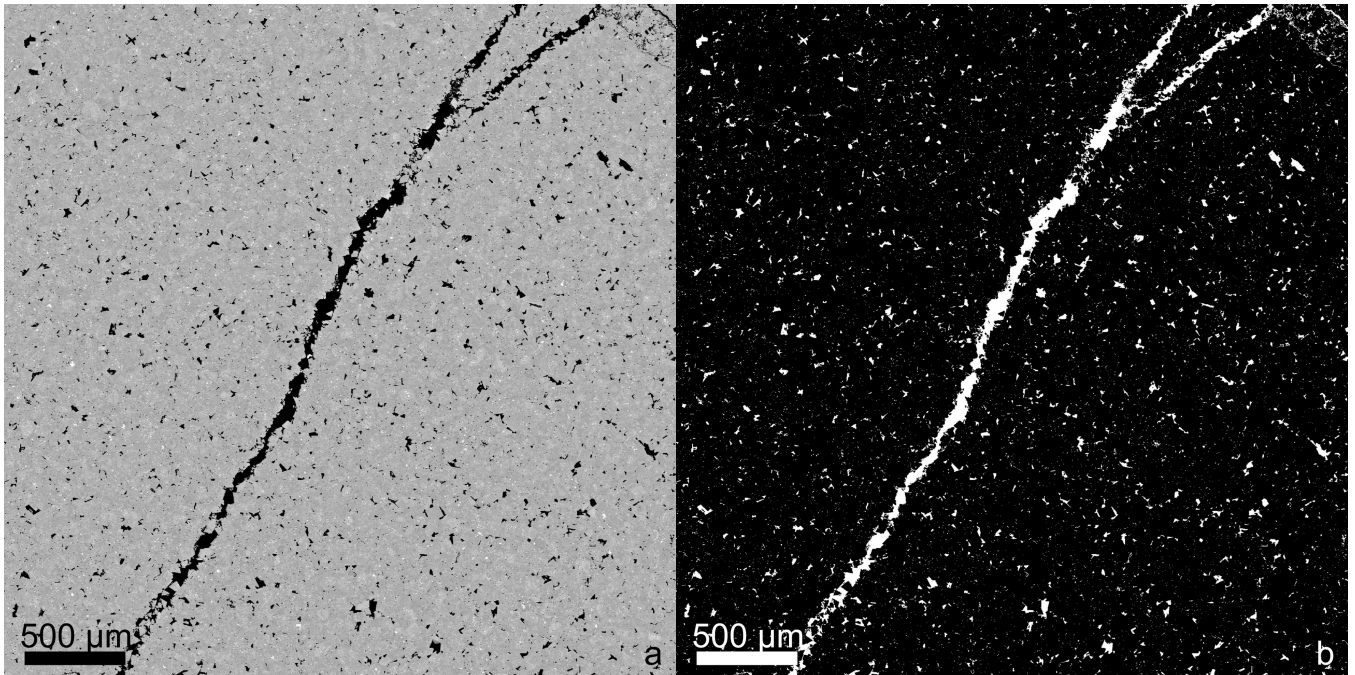
**Fig. 3.** Example of the *Local Thickness* approach for aperture determination on a fractured dolomite sample. a) 2D slice through a 3D binary segmented dataset of  $\mu$ CT data, at  $(18.9 \mu\text{m})^3$  per voxel resolution. b) Local aperture distribution, shown as a 2D slice of the same area of (a), taken from the full 3D processed dataset.



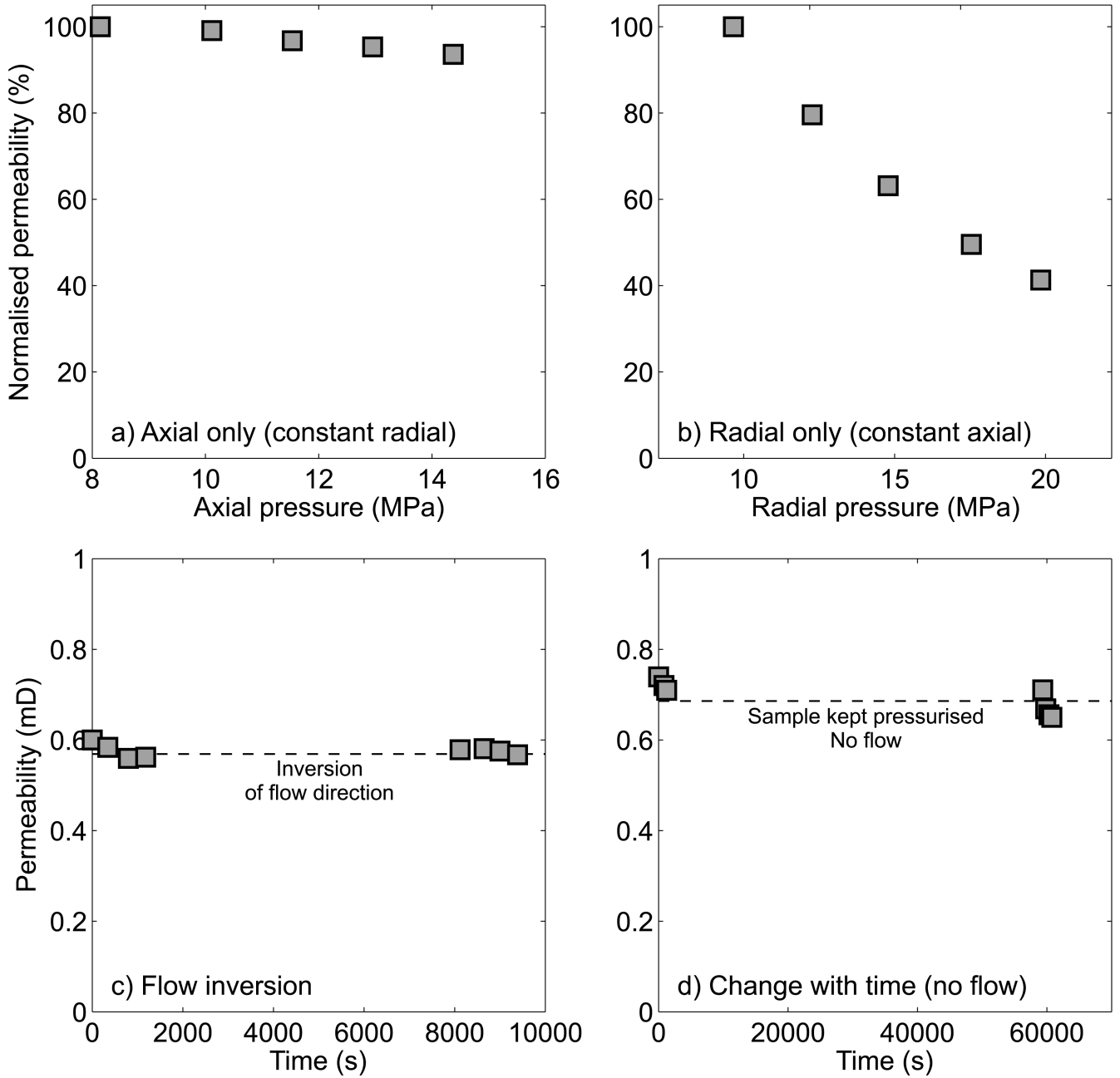
**Fig. 4.**

Comparison of  $\mu$ CT and thin section data on a fractured dolomite plug sample of 2 cm diameter (Prottes TS1-8sp). (a) and (c) are taken from a 2D slice through a 3D  $\mu$ CT dataset at  $(12.5 \mu\text{m})^3$  per voxel resolution. (b) and (d) show thin section SEM-BSE images at  $(1.45 \mu\text{m})^2$  per pixel resolution that have been (approximately) matched to the data in (a) and (c). The overview in (b) is a stitched result from 292 SEM-BSE images. Although large fractures, veins and brecciation are recognisable in the  $\mu$ CT data, the thin section data allows

a much more detailed analysis, e.g. on small pores, the internal structure of dolomite crystals, and the interaction between a calcite vein and the dolomite host rock.



**Fig. 5.** Example of the result of the Otsu method for global binary segmentation on a part of a thin section (sample Prottes TS1-8sp). a) Part of stitched SEM-BSE image data, corrected for global contrast and brightness variations. b) Part – corresponding to the area in (a) – of the Otsu threshold result on the complete stitched dataset. A porosity of 4.8% is obtained by this method for the complete stitched dataset (5.3% porosity in the example area shown here).

**Fig. 6.**

Response of permeability to changes in several parameters, for a water permeability experiment on a fractured dolomite sample. The measurements shown here represent single permeability measurements (i.e. one  $Q$  and  $DP$  in Equation 4.2). a) Permeability response to changes in axial pressure, at constant radial pressure of circa 7.4 MPa. b) Permeability response to changes in radial pressure, at constant axial pressure of circa 9.7 MPa. c) Influence of inverting the flow direction, while keeping all other parameters constant. d) Influence of time without flow. After the first series of measurements, flow was turned off, but all other parameters (confining pressure, pore fluid pressure) were kept constant for several hours. No significant change in permeability was observed when resuming flow.

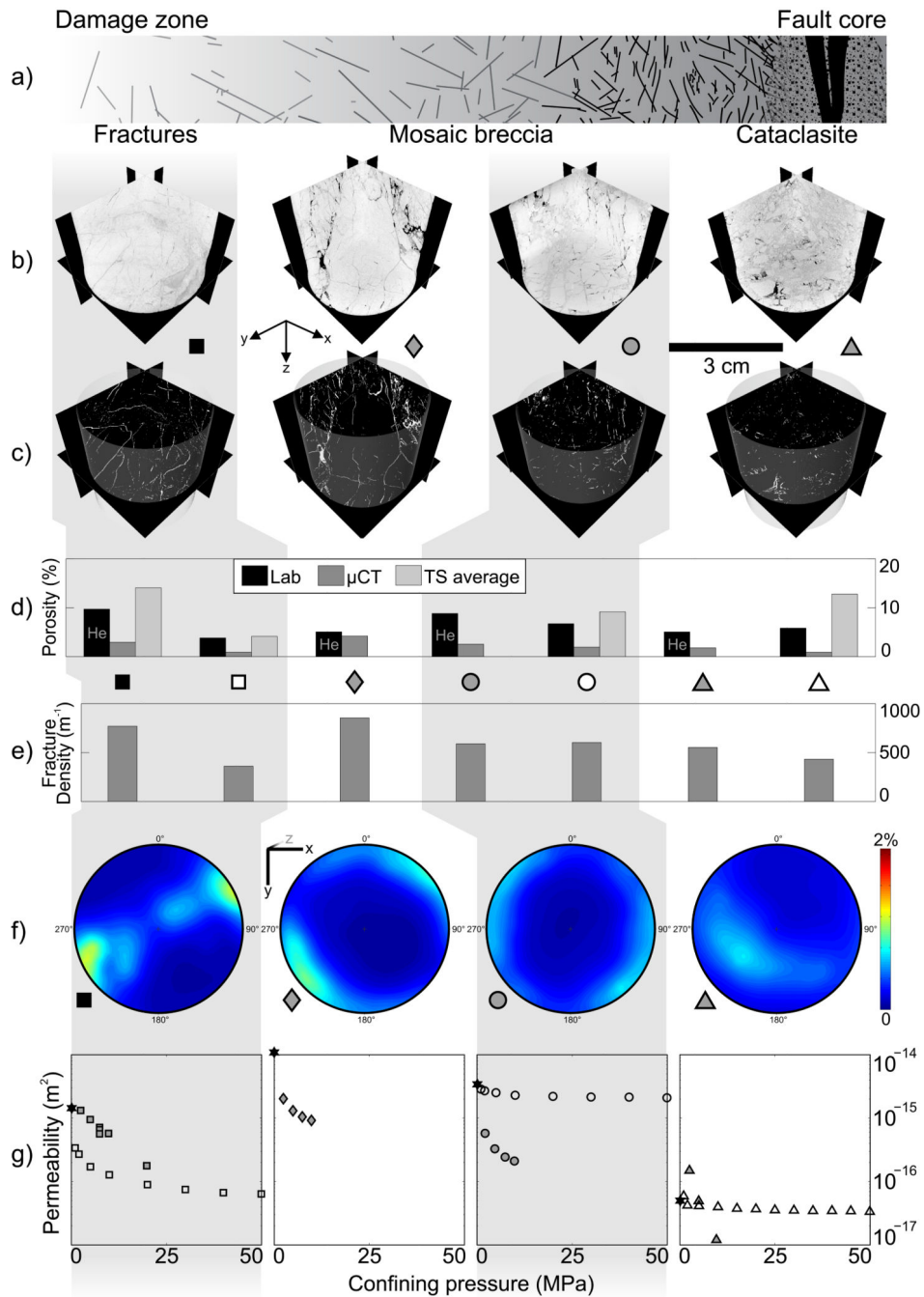


**Fig. 7.** Compilation of the main results of this study. The grey and white bands in the background divide four groups, from left to right: 1) fractured-only samples (squares), 2) mixture of fractures and breccias (diamond), 3) mosaic breccias (circles), and 4) cataclasites (triangles). Sample symbols as in table 2. See text in Section 5 for a detailed discussion. a) Fault zone structure as interpreted from fieldwork. b) Orthoslice based views through four 3D  $\mu$ CT datasets of 3 cm diameter plug samples, with reconstructed resolutions of (left to right):  $(18.9, 19, 19$  and  $20 \mu m)^3$  per voxel. c) Filtered and segmented results of the data in (b). d)

Bulk porosity for the different samples, from three different sources. Thin sections were not available for all samples. The laboratory values on the 3 cm samples are indicated by “He” (helium porosimetry). e) Fracture density. f) Examples for the samples in (a) and (b) of equal area, lower hemisphere projections of poles to fracture planes, determined at every porosity voxel in each dataset, and plotted to the same relative scale. N (left to right) =  $197 \cdot 10^6$ ,  $226 \cdot 10^6$ ,  $88 \cdot 10^6$  and  $91 \cdot 10^6$ . g) Permeability values during confining pressure loading experiments. Open symbols: gas permeabilities; filled symbols: water permeabilities. Gas permeability experiments without confining pressure (on the same samples with the closed symbols in each diagram) are shown as black stars.



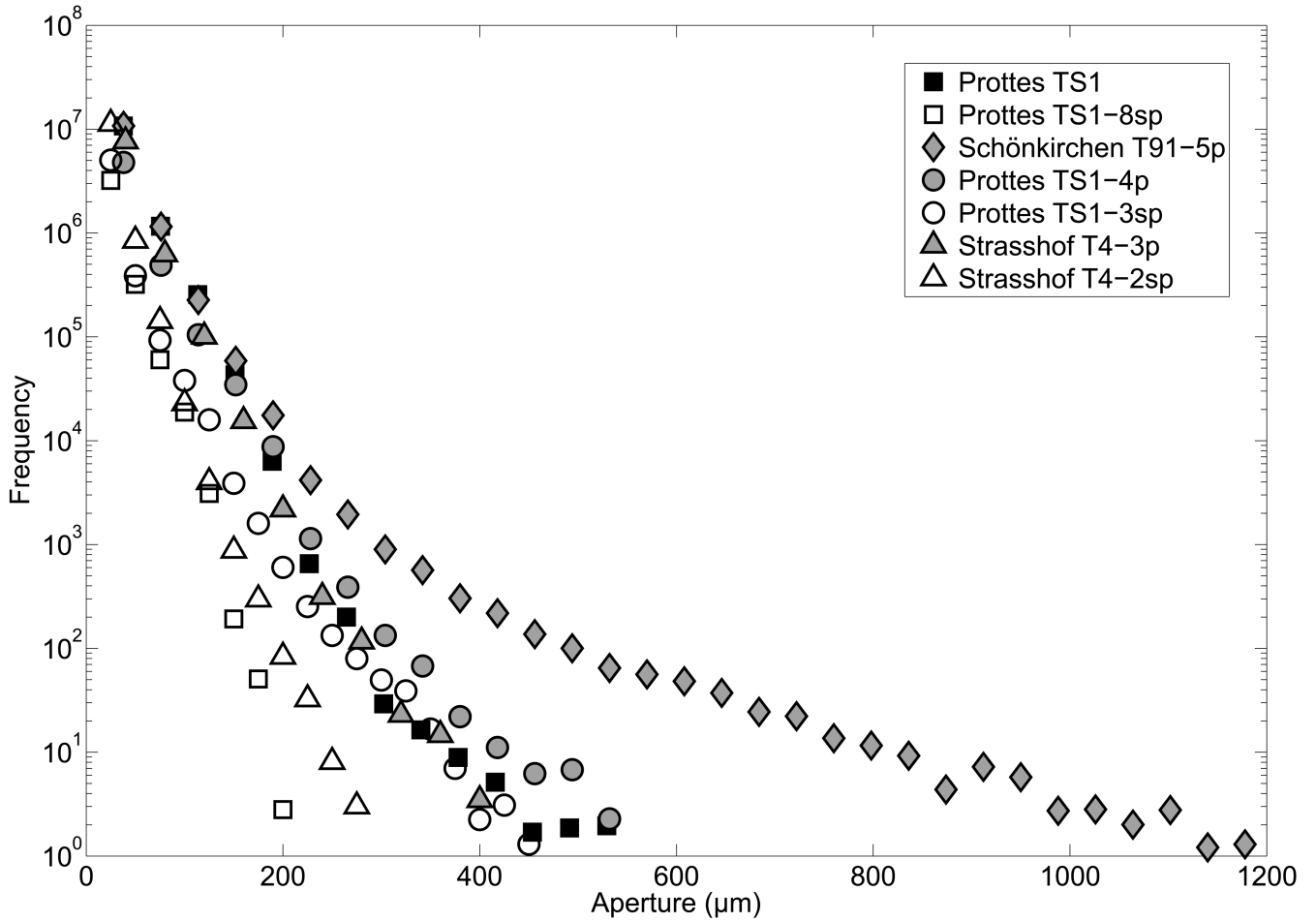


**Fig. 8.** Normalised aperture distributions determined from  $\mu\text{CT}$  data (symbols as in Table 2). The brecciated and fractured sample Schönkirchen T91-5p clearly stands out from the other samples, and 2 cm diameter samples (open symbols) consistently have smaller aperture distributions than the similar 3 cm diameter samples.

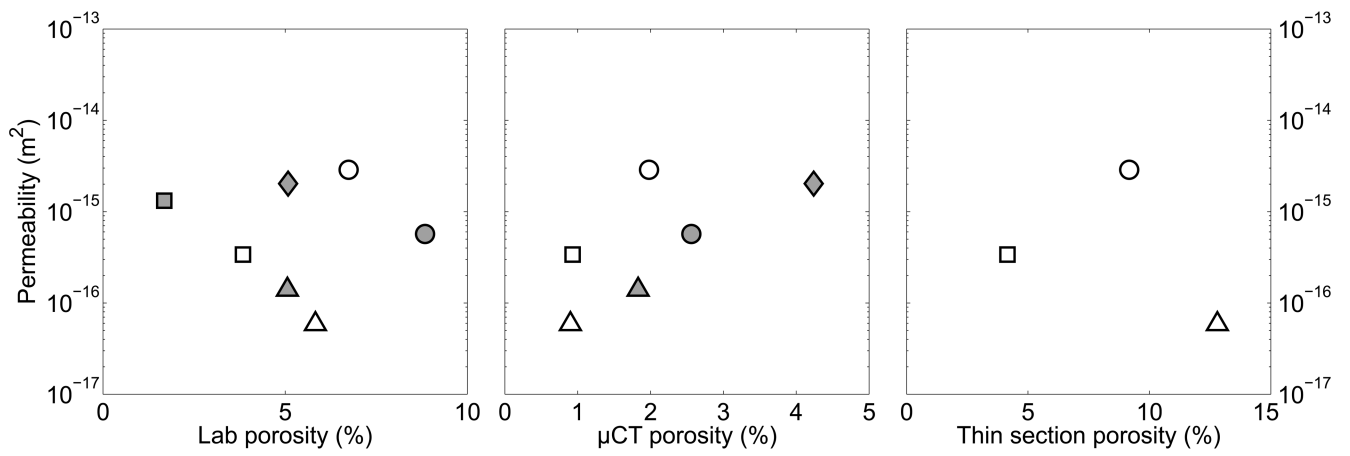


**Fig. 9.** Porosity to permeability relationship for the samples shown in this study (values and symbols in Table 2). The porosities chosen are from a) laboratory b)  $\mu$ CT bulk values c) thin section SEM-BSE porosities. For all three plots, no simple porosity-permeability relationship can be inferred.

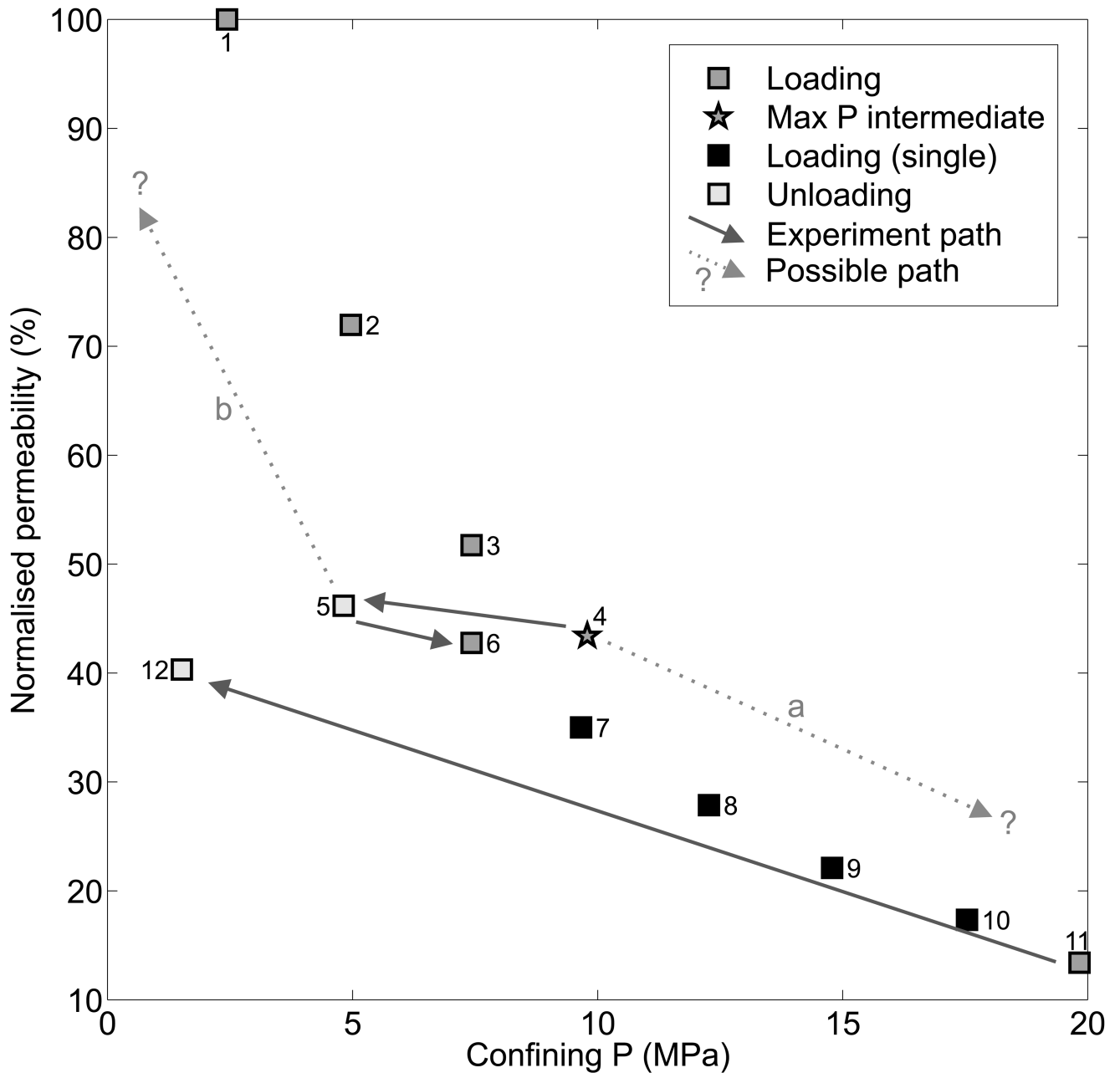


**Fig. 10.**

Permeability measurements on a dolomite plug sample containing a single fracture (Schönkirchen T32-430), during various loading and unloading stages with water permeability. The order of consecutive measurement steps is labelled by the numbers, and the order of loading and unloading has an influence on the final results. Steps 7-10 only represent one measurement at one flow rate (rather than 4 combined measurements). After loading to an initial maximum intermediate confining pressure (point 4), the sample was unloaded. However, if loading would have continued, the path shown by arrow a could be

expected. If unloading would have continued after point 5, possibly path b (as seen for the other samples) would have been followed.

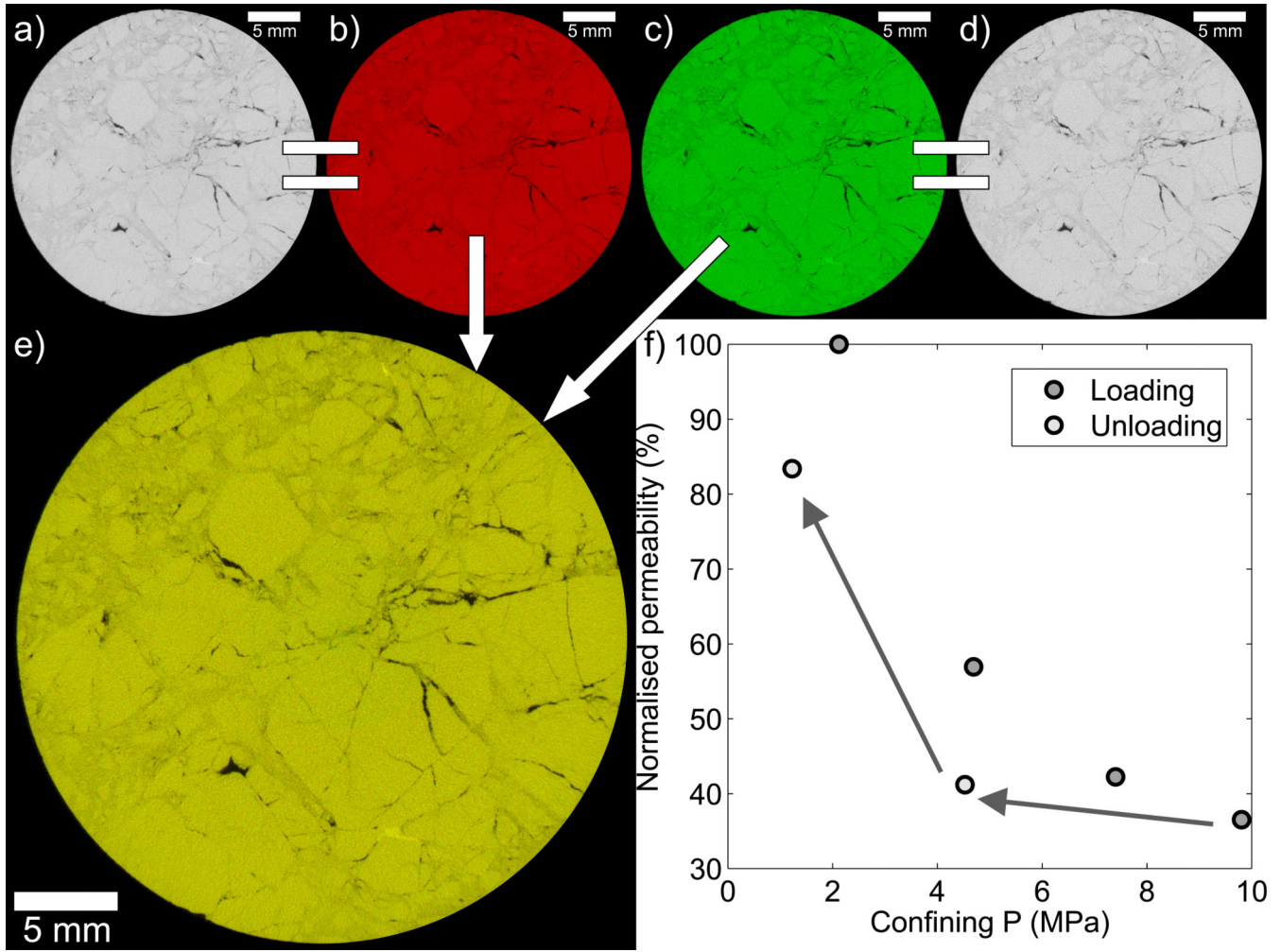


**Fig. 11.** 2D slices from  $\mu$ CT scans before (a) and after (d) a permeability experiment under confining pressure, on a 3 cm diameter plug (Prottes TS1-4p), reconstructed at a resolution of  $(15 \mu\text{m})^3$  per voxel. The scans before (a) and after (b) have been 3D registered to obtain a perfect match. b) Figure (a) with intensity set as red channel only. c) Figure (d) with intensity set as green channel only. e) RGB combination of (b) and (c), showing a perfect match of the two images. If clear differences between the scans would exist, they would show up as distinct green or red areas. f) Loading and unloading behaviour of the sample. After unloading, the permeability is lower than at the initial stage.

Table 1

Properties of samples scanned using  $\mu$ CT in this study

Sample	Dimensions ( $\emptyset$ (cm) * 1 (cm))	Depth (m) [1]	Fault zone interpretation [2]	Dolomite Texture [3]	Cements (veins and pores)	Clay content [4]
Prottes TS1	3.0 $\times$ 7.0	2795	Fractured (D)	Mainly subhedral with interstitial pores	Some calcite and pyrite pore filling and small veins.	High in matrix and along fractures.
Prottes TS1-8sp	2.0 $\times$ 2.2	2795	Fractured (D)	Mainly euhedral with interstitial pores	Large calcite veins, some pyrite veins. Locally abundant pyrite pore filling.	Some, mainly along fractures.
Schönk. T91-5p	3.0 $\times$ 5.7	3008	Fractured + mosaic breccia (D-C)	<i>Mainly nonplanar</i>	<i>Low pyrite content in matrix and fractures.</i>	<i>Abundant as pore and fracture filling, higher in brecciated parts.</i>
Prottes TS1-4p	3.0 $\times$ 2.2	2795	Mosaic breccia + cataclasite zones (C)	<i>Mainly euhedral with interstitial pores</i>	<i>Some calcite and pyrite pore filling and small veins.</i>	<i>Abundant in cataclasite zones.</i>
Prottes TS1-3sp	2.0 $\times$ 2.2	2795	Mosaic breccia + cataclasite zones (C)	Mainly euhedral with interstitial pores	Few calcite veins, low pyrite content in pores.	Abundant in cataclasite zones.
Strasshof T4-3p	3.0 $\times$ 7.0	3320	Embryonic-intermediate cataclasite (C)	<i>Nonplanar</i>	<i>Dolomite veins, possibly abundant. Low pyrite content in matrix.</i>	<i>Abundant in matrix.</i>
Strasshof T4-2sp	2.0 $\times$ 5.0	3320	Embryonic-intermediate cataclasite (C)	Nonplanar	Abundant dolomite veins and pore cements. Low pyrite content in matrix.	Abundant in matrix, some continuous bands.

*Italic* text means interpretation from  $\mu$ CT data or thin sections on a similar sample (not thin sections on sample itself). The terminology is followed after Flügel (2004).









[1] Minimum depth of core as reported on core boxes.

[2] D = damage zone, C = fault core.

[3] Classification scheme of Sibley & Gregg (1987).

[4] Main clay components: illite and kaolinite.

**Table 2**  
Samples, symbols, porosity, fracture density-porosity relationship, and permeability

Sample	Symbol [1]	Lab- $\Phi$ [2]	$\mu$ CT- $\Phi$	TS- $\Phi$ [3]	Fracture density / $\mu$ CT porosity	$\kappa$ (m <sup>-2</sup> ) [4]	Fault zone interpretation [5] and comments
Schönkirchen T32-430		1.7 % (He)	N.A.	N.A.	N.A.	1.3·10 <sup>-15</sup>	Fractured (D), no $\mu$ CT scan available
Prottes TS1		9.7 % (He)	3.0 %	14.1 %	259	N.A.	Fractured (D), no permeability data
Prottes TS1-8sp		3.8 %	0.9 %	4.2 %	389	3.4·10 <sup>-16</sup>	Fractured (D)
Schönkirchen T91-5p		5.1 % (He)	4.2 %	N.A.	202	2.0·10 <sup>-15</sup>	Fractured + mosaic breccia (D-C)
Prottes TS1-4p		8.9 % (He)	2.6 %	N.A.	230	5.7·10 <sup>-16</sup>	Mosaic breccia + cataclasite zones (C)
Prottes TS1-3sp		6.7 %	2.0 %	9.2 %	304	2.9·10 <sup>-15</sup>	Mosaic breccia + cataclasite zones (C)
Strasshof T4-3p		5.1 % (He)	1.8 %	N.A.	302	1.4·10 <sup>-16</sup>	Embryonic-intermediate cataclasite (C)
Strasshof T4-2sp		5.8 %	0.9 %	12.8%	481	5.9·10 <sup>-17</sup>	Embryonic-intermediate cataclasite (C)

[1] Closed symbols: 3 cm diameter samples, water permeability experiments under confining pressure (if available). Open symbols: 2 cm diameter samples, gas permeability experiments under confining pressure. The shape of the symbols refers to the fault zone interpretation, shown in the last column (repeated from Table 1).

[2] Porosities measured by Helium porosimetry are indicated by "He", the other porosities are measured by water saturation porosimetry.

[3] Thin section porosities, averaged out over several 2D thin sections taken from the plugs.

[4] Permeability at lowest confining pressure in the experiments under confining pressure. Plots of these permeability values against the three different porosity estimates are shown in Fig. 9

157 Fault zone classification as in Table 1; D = damage zone, C = fault core.